Open Access Theses

Theses and Dissertations

Summer 2014

Correlating Grain Size to Radiation Damage Tolerance of Tungsten Materials Exposed to Relevant Fusion Conditions

Sean Robert Gonderman
Purdue University

Follow this and additional works at: https://docs.lib.purdue.edu/open_access_theses

Part of the Materials Science and Engineering Commons, and the Nuclear Engineering Commons

PURDUE UNIVERSITY
GRADUATE SCHOOL
Thesis/Dissertation Acceptance

This is to certify that the thesis/dissertation prepared

By Sean Gonderman

Entitled
CORRELATING GRAIN SIZE TO RADIATION DAMAGE TOLERANCE OF TUNGSTEN
MATERIALS EXPOSED TO RELEVANT FUSION CONDITIONS

For the degree of   Master of Science in Nuclear Engineering

Is approved by the final examining committee:

Ahmed Hassanein

Anter El-Azab

Eric Kvam

Jean Paul Allain

To the best of my knowledge and as understood by the student in the *Thesis/Dissertation Agreement. Publication Delay, and Certification/Disclaimer (Graduate School Form 32)*, this thesis/dissertation adheres to the provisions of Purdue University's "Policy on Integrity in Research" and the use of copyrighted material.

Ahmed Hassanein

Approved by Major Professor(s): _____

Approved by: Ahmed Hassanein   07/25/2014

Head of the Department Graduate Program   Date

CORRELATING GRAIN SIZE TO RADIATION DAMAGE TOLERANCE OF TUNGSTEN

MATERIALS EXPOSED TO RELEVANT FUSION CONDITIONS

A Thesis

Submitted to the Faculty

of

Purdue University

by

Sean Gonderman

In Partial Fulfillment of the

Requirements for the Degree

of

Master of Science in Nuclear Engineering

August 2014

Purdue University

To my loving wife and my supporting parents; thank you for giving me this opportunity

TABLE OF CONTENTS

LIST OF TABLES

LIST OF FIGURES

ABSTRACT

Gonderman, Sean Robert. M.S.N.E., Purdue University, August 2014. Correlating Grain Size to Radiation Damage Tolerance of Tungsten Materials Exposed to Relevant Fusion Conditions. Major Professor: Jean Paul Allian.

Tungsten remains a leading candidate for plasma facing component (PFC) in future fusion devices. This is in large part due to its strong thermal and mechanical properties. The ITER project has already chosen to use an all tungsten divertor. Despite having a high melting temperature and low erosion rate, tungsten faces a large variety of issues when subject to fusion like conditions. These include embrittlement, melting, and extreme morphology change (growth of fuzz nanostructure). The work presented here investigates mechanisms that drive surface morphology change in tungsten materials exposed to fusion relevant plasmas. Specifically, tungsten materials of different grain sizes are studied to elucidate the impact of grain boundaries on irradiation damage.

Exposure of ultrafine (< 500 nm) and nanocrystalline (< 100 nm) grain materials are exposed to high flux helium plasmas at the Dutch Institute for Fundamental Energy Research (DIFFER) in the Netherlands. These samples are then compared to large grain (1-5 microns) tungsten materials exposed to similar conditions at DIFFER or tungsten

samples from other published studies. After exposing the ultrafine grain materials to a variety of helium plasmas to different fluences between 1 x 10^{23} – 1 x 10^{27} ions-m^{-2}, temperatures between 600-1500 °C, and ion energies between 25-70 eV, it is observed that ultrafine grained tungsten samples develop fuzz at an order of magnitude larger fluence when compared to large grained tungsten. These observations suggest that grain boundaries play a role in dictating damage accumulation and damage rate caused by ion bombardment of tungsten surfaces.

These experiments are complemented by In-situ TEM analysis during 8 keV Helium irradiation of ultrafine tungsten samples to see damage propagation in different sized grains in real time. The in-situ TEM work was completed in a JEOL JEM-2000FX TEM at the Microscope and Ion Accelerator for Materials Investigation (MIAMI) facility at the University of Huddersfield. The TEM results show a strong dependence on grain size and defect production rate. Images also suggest that smaller grains tend to form helium bubbles at the grain boundaries. The distribution of bubble size and location is significantly different in nanocrystalline grains

CHAPTER 1.   INTRODUCTION

1.1   <u>Motivation</u>

Research for fusion devises for energy production is being led by the ITER project. The objectives of ITER include demonstrating the feasibility of fusion as a commercial energy source and providing an environment to test fusion technologies for the future [1]. This calls for additional research on the components that will comprise the ITER device. One area that needs further investigation is Plasma Facing Components (PFCs). The PFCs will be subjected to neutron and ion bombardment coupled with high heat fluxes, and the response of these materials can have a large impact on the plasma performance of the device [2,3]. For example, sputter yield of the PFC material is an important parameter because it affects the amount of impurities that enter the plasma from the walls. These impurities have a negative impact on both the plasma temperature (T_i) and the plasma density (n_e) [4,5]. Thus, it is necessary to study the Plasma Surface Interaction (PSI) of candidate materials to be used in future fusion devices like ITER.

1.2   Tungsten as a PFC

1.2.1   Tungsten thermal and mechanical properties

Tungsten has come to the forefront as a prime material for use in fusion devices because of several key thermal properties [2, 3, 6]. First, the melting point of tungsten is 3410 °C [7]. This is desirable because the estimated peak power flux ($q_{\perp, peak}$) for normal operation is estimated to be ~ 10 MW/m^2, which would correspond to a peak surface temperature of ~1100 °C [3]. It is worth noting the 1100 °C is still below the recrystallization temperature of Tungsten. However, plasma disruptions like edge localized modes (ELMs) have the potential to push the heat flux up to several GW/m^2,which would increase the peak surface temperature past the melting point of Tungsten[8]. In addition to the high melting point of tungsten, it also has high thermal conductivity [3] and high temperature strength [2].

1.2.2   Tungsten sputtering properties

As mentioned before, impurities from the wall can enter the plasma at a relatively cold temperature through erosion induced by irradiation. These impurities lower the plasma temperature by radiative cooling, which is a function of atomic number (Z)[9]. Thus, impurities with a greater mass will have a more detrimental effect on the plasma.

Despite tungsten being a high Z material (Z=74), it can still be used as a PFC due to its low erosion rates. This is due to the sputter threshold for tungsten be 160-210 eV [10] for deuterium ions (D+) and about 200 eV [11] for Helium ions (He+). Below is a figure taken from R. A. Pitts et al. [12] which details the difference in sputter yield due to physical sputtering among various PFC materials.
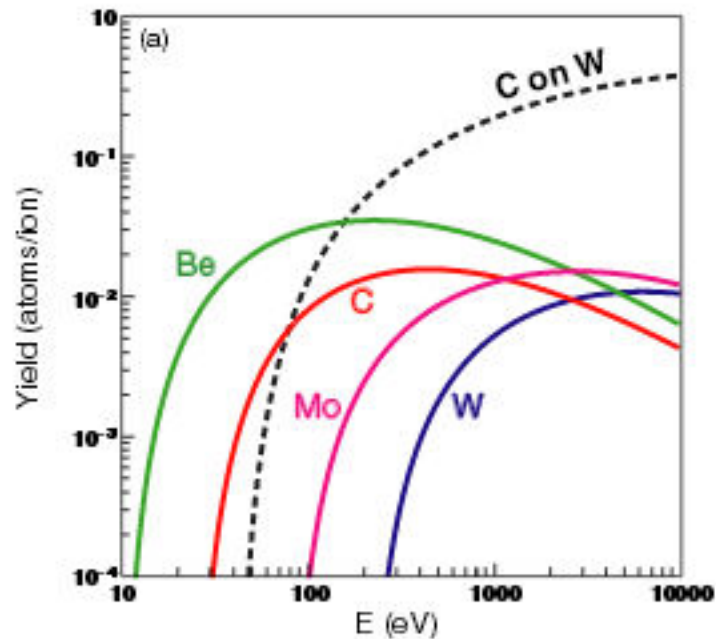
Figure 1.1: Sputter yield for PFC materials undergoing physical sputtering via deuterium irradiation at normal incidence.

Figure 1.1 details why tungsten exhibits lower erosion due to a higher physical sputtering threshold. This low erosion leads to less radiative cooling and a more desirable PFC. Other sputtering mechanisms like self-sputtering [13] and chemical sputtering [14] play a major role in erosion of tungsten PFCs as well. The magnitude of self-sputtering sputter yield is more strongly dependent on edge plasma temperature

than that of physical sputtering. This requires the edge plasma temperature to be held

around 25 eV to keep tungsten erosion at an acceptable level [13].

1.2.3 Neutron irradiation of tungsten

Tungsten is a bcc metal and therefore subject to embrittlement via neutron

irradiation [15]. This can raise the ductile to brittle transition temperature (DBTT)

causing the material to crack and fail more easily than expected. This increase in DBTT

via irradiation can be suppressed with alloying, but more studies are needed to

investigate the effect that alloying would have on properties such as sputtering which

greatly influence the plasma condition [2]. A study conducted by Steichen et al. [16]

showed that mechanical properties of tungsten change drastically when subjected to

neutron irradiation. Tungsten samples were exposed to fluences of $0.5 - 0.9 \times 10^{22}$

neutrons-cm^{-2}. This caused an increase in strength but a decrease in ductility in the

tungsten samples. Steichen reports brittle fractures at stresses 5-10 times lower then

observed in the unirradiated cases [16]. The study by Davis et al. [2] investigates several

different designs to help mitigate this issue. One idea is to use small tungsten bars,

plates or rods that are embedded into a copper cast. The copper cast is soft and yields

easily. This lowers the residual stresses in the tungsten that occur due to irradiation

effects like swelling [2].

Another study by Shimada et al. [17] investigated the effect of neutron

irradiation on the retention of hydrogen in tungsten. Pure tungsten samples were

irradiated by neutrons at 50 °C to 0.025 dpa at the High Flux Isotope Reactor at Oak

Ridge National Lab. The neutron irradiated samples were then exposed to a high flux

deuterium plasma at the Tritium Plasma Experiment at Idaho National Lab [17]. The

deuterium flux range was $10^{21} - 10^{22}$ ions-m^{-2}-s^{-1}, the fluence range was $10^{25} - 10^{26}$ ions-

m^{-2}, and the temperature range was 100-500 C [17]. Figure 1.2 shows the deuterium

depth profiles for neutron irradiated and unirradiated tungsten at different

temperatures.
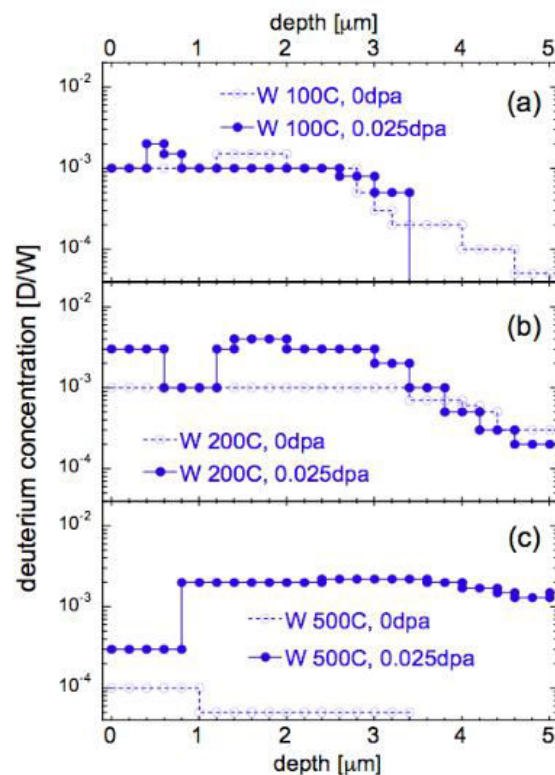
Figure 1.2: Deuterium depth profiles in 0 and 0.025dpa tungsten. Image and caption taken from Shimada et al. [17].

Figure 1.2 shows a significant difference in deuterium trapping caused by neutron

irradiation. This difference is largest in the 500 C case.

Neutron irradiation has a detrimental effect on the mechanical properties of tungsten. Embrittlement of tungsten under neutron irradiation may cause mechanical failure in fusion devices. In addition to mechanical concerns, neutron irradiation also has an effect on retention of tritium and deuterium in tungsten PFCs.

1.3   Chapter Summary

Tungsten is a desirable candidate for a PFC because of its good thermal properties and low erosion. However, neutron irradiation of tungsten has been shown to change the mechanical properties and the retention properties in an adverse way. Failure due to embrittlement and higher retention are major engineering concerns for tungsten as a PFC in future fusion devices. In addition to these issues, continued research into tungsten has shown it undergoes severe morphology change when exposed to helium and deuterium irradiation. These induced changes effect deuterium retention, erosion and the mechanical properties of tungsten as well. Ongoing research is focused in understanding the surface evolution process and its subsequent effects on these key properties. The following chapter will discuss current research regarding the effects of helium and deuterium irradiation on tungsten surfaces. This will be followed by the focus of this thesis, which looks specifically at tungsten materials of different grain sizes and elucidates the role grain boundaries play in irradiation tolerance for potential tungsten PFCs.

CHAPTER 2.   TUNGSTEN MORPHOLOGY EVOLUTION IN FUSION DEVICES

Morphology evolution of tungsten surface via irradiation has been shown to form a nano-tendril (fuzz) structure in many linear plasma device studies [18,19,20]. A recent study performed at Alcator C-Mod showed that this fuzz structure can also be formed in a tokomak device [21]. This tungsten morphology change is induced from both He+ and D+ irradiation, and both of these species will be present in future fusion devices. This gives motivation to fully understand the mechanisms that cause this structure change and to determine the resulting impact on plasma conditions.

2.1   Tungsten surface response to deuterium irradiation

A large number of studies have been conducted on understanding the effect that deuterium irradiation has on tungsten surface morphology, and how that resulting morphology change effects key material parameters such as retention and sputter yield [22,23,24,25,26].

2.1.1   Effect of ion energy on blistering during deuterium irradiation

A study conducted by Luo et al. [26] showed evidence of blister formation on

tungsten surfaces when exposed to deuterium irradiation with ion energies ranging

from 7 -98 eV. Figure 2.1, showing the critical fluence for blister formation as a function

of incident ion energy, is shown below.
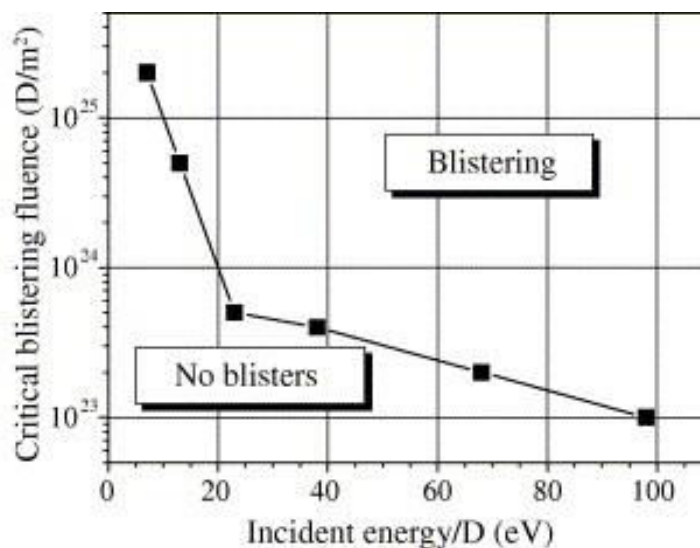
Figure 2.1: Critical fluence for blister formation in tungsten as a function of incident ion energy [26].

Figure 2.1 shows the fluence at which blisters were observed for deuterium irradiations

at room temperature and an ion flux of ~1×10^{22} D+/m^2-s. The turning point in figure 2.1

is thought to be due to a chemical effect brought about by the formation of W-O

complexes during the irradiation processes. This thin oxide layer inhibits the penetration

of the deuterium items into the surface [26]. This study shows that blistering does occur

within the incidentent ion energy range expected in ITER [26], but it does not look at the

role of other effects, like temperature, on the surface evolution of tungsten. Additional

studies by Tokunaga et al. [23] and Wang et al. [22] look more closely at temperature

effects on blister formation and the resulting retention of deuterium. Figure 2.2 below is

from the Wang et al. study, and it shows the difference in surface morphology as a

function of temperature using Scanning Electron Microscopy (SEM) micrographs.
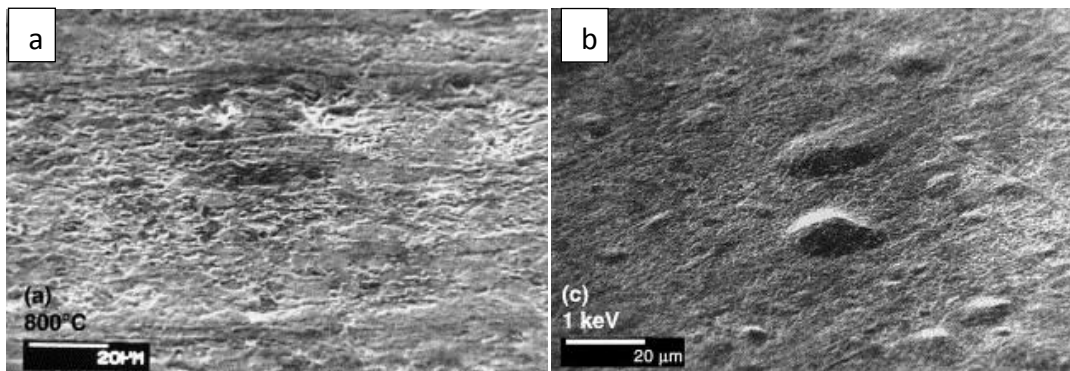
Figure 2.2: SEM images of tungsten samples bombarded by 1 keV D$^+$ up to the
fluence of 1×10^{21} cm^{-2} at different temperatures. (a) at 800 °C with scale bars of
20 μm, and (b) at RT with a scale bar of 1 μm [22].

Figure 2.2(b) shows no blisters while figure 2.2(c) show blisters. This implies that the

increased temperature is suppressing the blister formation mechanism. In addition to

the temperature dependence of blister formation, Wang et al. also compiled results on

erosion yields of tungsten surfaces as a function of fluence, ion energy, and temperature.

This is shown in table 2.1 [22].

Table 2.1: Erosion yield of W and D ion bombardment as obtained from weight loss measurements. Table and caption taken from Wang et al.[22].

Energy (eV)	Fluence (D$^+$/cm^2)	Yield at		
		20 °C	600 °C	800 °C
1000	1 × 10^{21}	2.87 × 10^{-3}	4.1 × 10^{-3}	3.65 × 10^{-3}
		2.85 × 10^{-3}		
	1 × 10^{20}	2.47 × 10^{-3}		
	After He prebomb.	2.5 × 10^{-3}		
	1 × 10^{19}	(1.1 ± 1) × 10^{-3}		
200	1 × 10^{21}	1.9 × 10^{-4}		
	1 × 10^{20}	<1 × 10^{-4}		
100	1 × 10^{21}	<7 × 10^{-5}		8.4 × 10^{-4}
		<5.3 × 10^{-5}		

The erosion data presented in Table 2.1 is determined from mass loss given by an *in-situ* microbalance with a sensitivity of up to 1 µg. This data shows a slight temperature dependence on erosion and a strong ion energy dependence on erosion. These results were found under low flux conditions of ~10^{20} m^{-2} s^{-1}, which is relevant for first wall studies but too low to recreate diverter conditions [22].

2.1.2 Effect of deuterium irradiation on retention properties of tungsten

High flux studies on these deuterium phenomena were conducted by Tokunaga et al. [23]. Their results also suggested a temperature dependence on the blister formation mechanism. This temperature dependence on blister formation due to deuterium irradiation seems to be coupled to the deuterium retention near the surface. Figure 2.3 shows the retention of deuterium as a function of temperature [23].
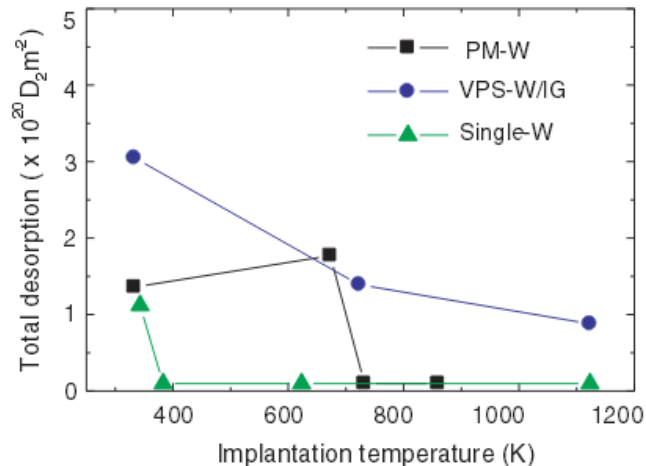
Figure 2.3: This is the total amount of desorption as function of irradiation temperature. The three types of tungsten presented here are powder metallurgy tungsten (PM-W), vacuum plasma spray tungsten (VPS-W) and single crystal tungsten (SC-W) [23].

Figure 2.3 looks at the retention of deuterium in several different tungsten materials, but the trend is consistent. The higher the temperature, the less retention is observed. This trend mirrors the blister behavior in that there is significantly less deuterium retained in samples where no blisters have formed, which suggests a link between blister formation and the deuterium retention mechanisms. The implication is that material design which controls blister formation, can be used to control retention properties in the material as well [23]. Further results from V. Alimov et al. [24] again support the observation that low energy D+ irradiation blisters are not seen at temperatures above 700 K. However, this study also investigates the role of He seeded plasma has on deuterium retention. Figure 2.4 shows the retention differences between tungsten samples exposed to pure D+ plasma and D-He plasma [24].
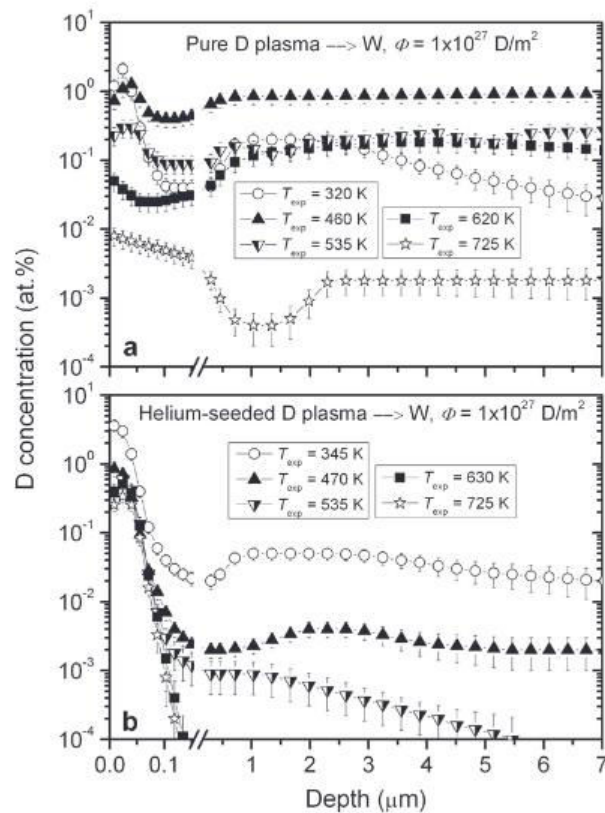
Figure 2.4: Depth profiles of deuterium retained in re-crystallized W exposed to pure D plasma (38 eV D^{-1}) (a) and helium-seeded D plasma (38eVD^{-1}+76 eV He^{-1}, 5% of He ions) (b) with a D ionfluence of 10^{27} D m^{-2}at various temperatures [24].

Figure 2.4 details the depth profile of deuterium concentration for both the pure

deuterium (a) and helium seeded (b) plasma cases. It is readily seen that there is a sharp

decrease in deuterium retention for the case in which helium seeded deuterium plasma

was used. However, it seems that the reduced retention effect is only prevalent in cases

above 350 K.

2.2   Tungsten surface response to helium irradiation

In addition to deuterium ions, PFCs will be exposed to substantial helium ion fluxes. These ions will be relatively low energy, in the tens of eV, but will still have a major impact on the evolution of the material surface despite being below the sputter threshold for helium on tungsten. A large number of studies have been conducted on the effects of He+ bombardment on tungsten as a PFC. These studies have focused on morphology evolution [27, 28, 29, 30, 18, 31, 32], *In-situ* analysis for understanding key mechanisms [33, 34], effect on retention properties [35], and investigating the response of different tungsten materials [36, 37].

2.2.1   Helium irradiation on tungsten at low fluence

PFCs are expected to undergo irradiation via neutrons, hydrogen isotopes, and helium ions ranging from 10 eV to several keV [27]. It has been shown that the helium irradiation effects are stronger than the hydrogen effects with regards to surface morphology change [38]. This has prompted a more focused investigation of the effects of He ion irradiation on tungsten microstructure evolution. A study by Iwakiri et al. [27] used *In-situ* TEM to investigate the resulting damage induced via 8 keV and 0.25 keV helium ions. Figure 2.5(a) shows TEM images of the 8 keV irradiations and figure 2.5(b) shows TEM images of the 0.25 keV irradiations.
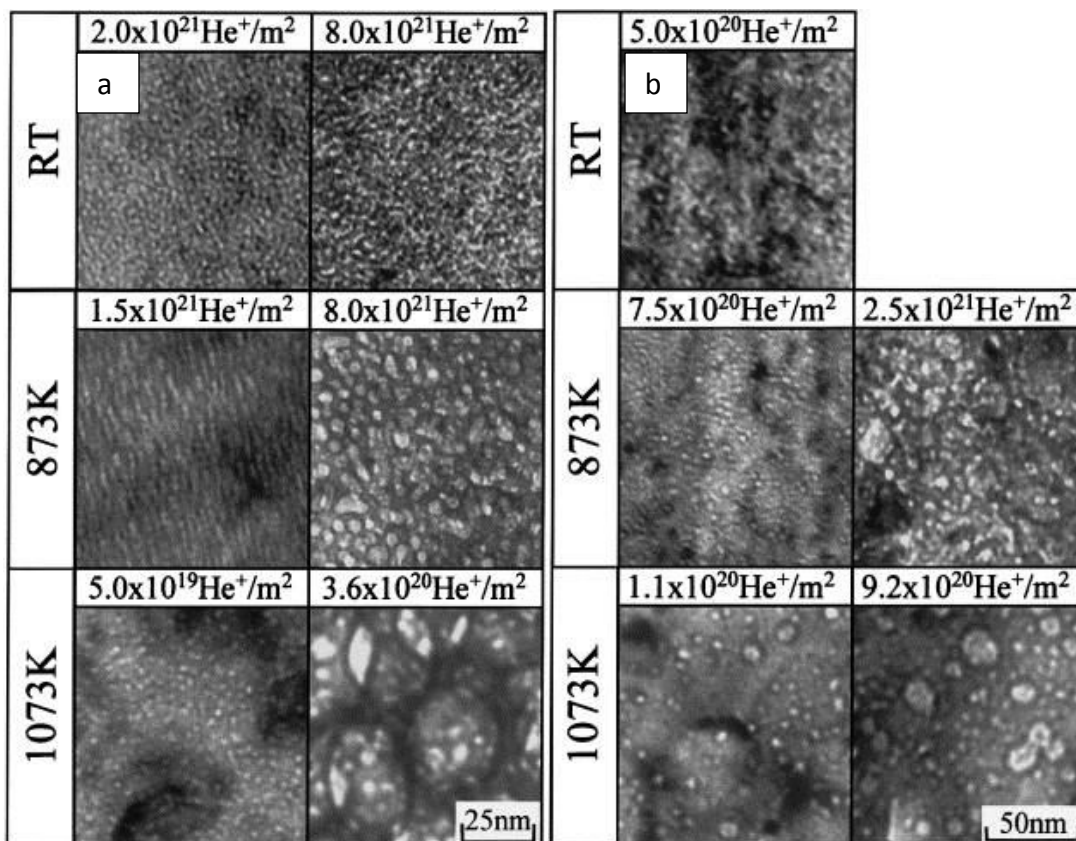
Figure 2.5: a) Temperature dependence of bubble formation during irradiation with 8 keV He$^+$ ions [27]. b) Temperature dependence of bubble formation during irradiation with 0.25 keV He$^+$ ions [27].

Iwakiri et al. [27] discusses how helium ion irradiation causes that formation of interstitial loops by trapping interstitials near helium-vacancy complexes, which was first shown in the following studies [39, 40]. The irradiation process forms He_iV_j complexes of various sizes, where i and j are the number of He atoms and vacancies associated with that complex respectively [41]. As more helium is trapped at these complex sites, the He-Vacancy complex can evolve by ejecting an interstitial into the surrounding matrix and becoming a complex with an additional vacancy [42]. These complexes continue to

grow resulting in the formation of interstitial loops. These loops are very stable which

explains why they are still observed at high temperatures [27]. This is in sharp contrast

with deuterium irradiation, which was shown earlier to not for form these loops at

higher temperatures. This loop formation mechanism is the seeding for the damage

seen in figure 2.5. In figure 2.5(a), 8 keV He ions were used, which is high enough energy

to incorporate knock-on damage to induce vacancies and create He-vacancy complexes

[27]. As temperature increases, so does vacancy mobility resulting in faster bubble

formation. In figure 2.5(b) the He ion energy was only 250 eV where knock-on damage is

not expected to occur. In these cases, a different mechanism for the formation of He-

Vacancy complexes is purposed by Iwakiri et al. [27]. Impurity atoms and self-

interstitials have been shown to strongly trap He atoms [43]. As these sites trap more

and more He atoms, the site can become unstable and force a nearby atom, out

creating a He-Vacancy complex, which proceed as normal [27].

This damage mechanism is further confirmed by Yoshida et al. [28]. In this study,

low energy He irradiation damage is further investigated. Yoshida et al. cites the low

migration energy for interstitials of 0.08 eV for tungsten allows for the formation of

dislocation loops even at room temperature. As the temperature of the irradiation

increases, the number of bubbles is observed to decrease but the size of these bubbles

increases. This change is observed for temperatures above 1073 K, where thermal

migration of vacancies is expected to take place [28]. Figure 2.6 shows the noticeable

difference in bubble size after 1073 K.
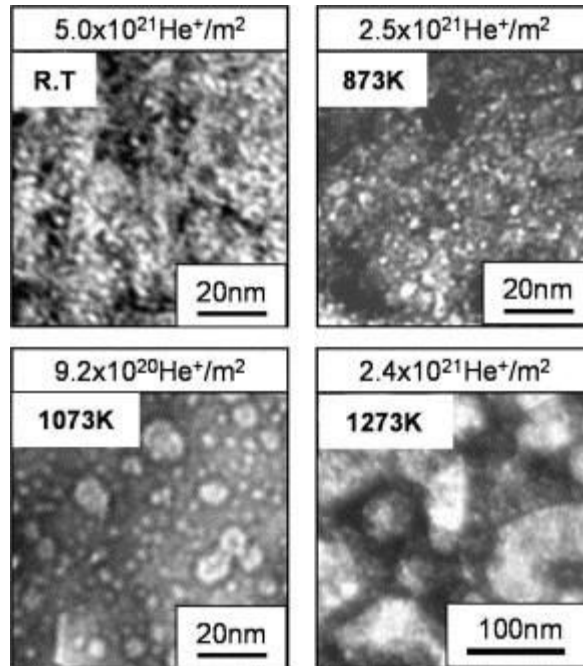
Figure 2.6: Temperature dependence of bubble formation in tungsten due to 0.25 keV He^+ irradiation [28].

Figure 2.6 shows very little difference in bubble size from the room temperature case to the 873 K case. However, the 1073 K and the 1273 K cases show much larger bubbles. This supports the conjecture that the size of the bubbles formed during the irradiation process has important factors that are thermally activated. In addition to temperature effects on bubble formation, a study by Nishijima et al. [30] showed an ion energy dependence on bubble formation. Figure 2.7 is a graph that looks at bubble formation as a function of incident ion energy and fluence/surface temperature.
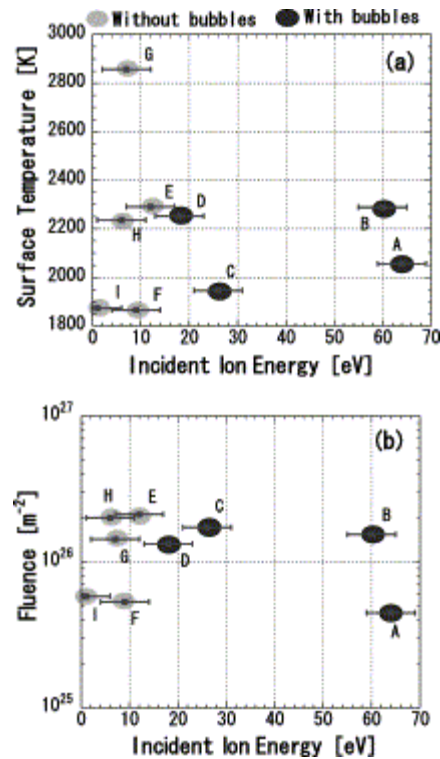
Figure 2.7: Summary of experimental conditions with and without bubble formation in the parameter spaces of (a) incident ion energy E_{in} and surface temperature T_s, (b) incident ion energy and fluence [30].

From this image, it appears that there is a minimum energy of ~15 eV needed to begin seeing bubbles. This threshold appears to hold versus fluence and temperature. This threshold is thought to be due to a surface barrier potential, which prevents He ions less then ~15 eV from penetrating into the material [30].

2.2.2   Helium irradiation on tungsten at high fluence

All of this work on He bubble formation has been at low fluences around 10^{21}-10^{22} ions/m^2. To see how these defects would drive surface evolution in fusion devices,

higher fluence studies were conducted. A paper by Kajita et al. [18] observed the growth

of a tendril-like nanostructure (Fuzz) on tungsten surfaces when exposed to helium

plasma under fusion relevant conditions. Figure 2.8 shows SEM and cross-sectional SEM

images of the development of this microstructure as a function of fluence.
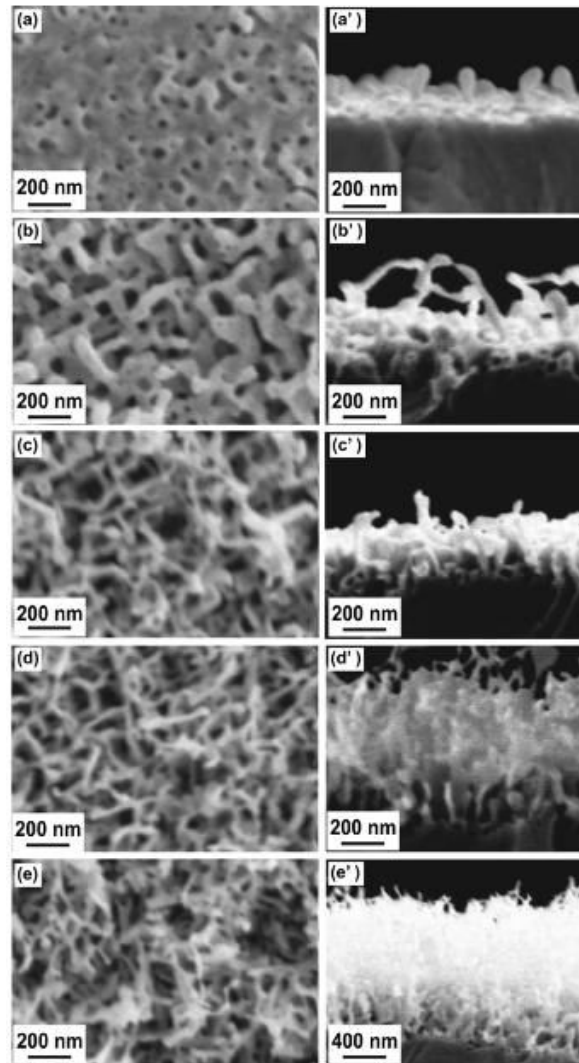
Figure 2.8: SEM images (a-e) and SEM cross-sectional images (a'-e') of tungsten samples exposed to different 50 eV He+ fluences at 1400 K. a) $6x10^{24}$ m^{-2} , b) $1.1x10^{25}$ m^{-2} , c) $1.8x10^{25}$ m^{-2} , d) $2.4x10^{25}$ m^{-2} , e) $5.5x10^{25}$ m^{-2} [18].

As seen in figure 2.8, long He exposures drastically change the surface. In figure 2.8(a) a

porous surface is observed, which is likely due to the formation of Helium bubbles

coming to the surface and rupturing. As more He bubbles continue to form, migrate and

burst, these pitting structure continues to evolve into the 'fuzzy' structure seen in figure

2.8(c)-2.8(e) [18]. It is also evident that the longer the surface is exposed the thicker the

fuzz region observed. A paper by Baldwin et al. [44] suggests that the growth follows a

$t^{1/2}$ dependence, where t is the time of the exposure to the He plasma. This is assuming

that the flux is above a minimum threshold value [44]. The $t^{1/2}$ dependence is thought to

arise from the simple 1-D growth law, d = $(2Dt)^{1/2}$, where D is the effective diffusion

coefficient, and a thermal activation energy is assumed to be 0.71 eV [44]. Figure 2.9

shows a plot of fuzz thickness vs $t^{1/2}$ for two sets of experiments at two different

temperatures.
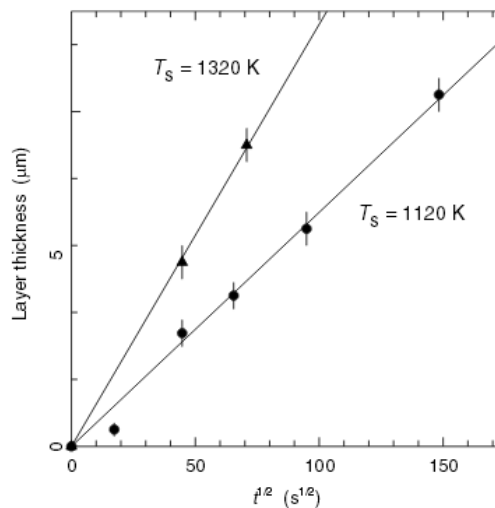
Figure 2.9: This is a plot of the observed fuzz thickness vs. the square root of the time exposed to He irradiation for temperatures of 1120K and 1320 K. The lines correspond the predicted fuzz thickness based on the assumption that the growth is dominated by 1-D diffusion [44].

Figure 2.9 shows good agreement between the 1320 K and 1120 K cases and the $t^{1/2}$ dependence. However, exposure time does not take into account flux. A more detailed study on the flux effect on fuzz thickness is still needed.

A map of the parameter space which is important to fuzz formation was purposed by Kajita et al. [18] by gathering relevant data from NAGDIS-II and PISCES-B machines and is shown in figure 2.10.
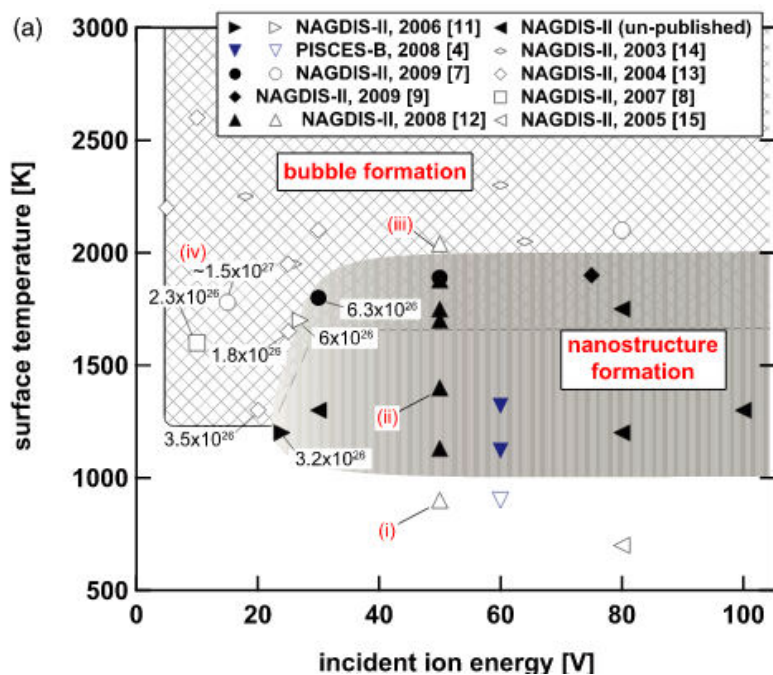
Figure 2.10: This is a figure taken from Kajita et al. [18] which show a parameter map of where nanostructure formation has been seen on W materials exposed to plasmas using the NAGDIS-II and PISCES-B machines.

Figure 2.10 shows several interesting features regarding the formation of fuzz. First, there is an ion energy dependence. This is not surprising, as we saw a similar ion energy dependence on the formation of He bubbles. Second, there is a temperature barrier at

around 1000 K, below which fuzz is not observed. This creates a fairly wide regime in

which fuzz formation is expected to occur.

2.2.3   *In-situ* TEM analysis of fuzz formation

The use of *in-situ* TEM has been employed by several studies to elucidate the

formation mechanisms of this fuzz nanostructure [45, 46]. *In-situ* TEM provides real time

information about the nature of defect production induced via He irradiation, as well as

information about how these defects interact and migrate in the material. Figure 2.11 is

an image that captures the evolution of several He bubbles which lead to the formation

of a tendril or fuzz-like structure.
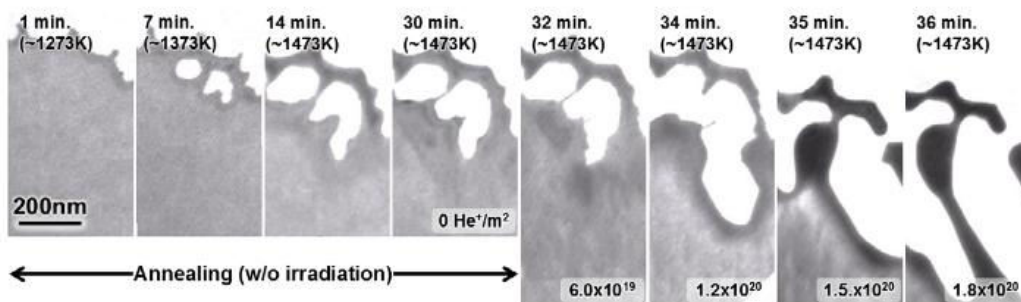
Figure 2.11: The first four frames show the annealing process as the sample is heated to 1473 K. The following frames show the rapid change in shape and size of these voids due to He+ irradiation [46].

This real time evolution of the surface matches theories proposed by Kajita et al. [45]

regarding the fuzz growth process. a) In the initial stage Helium bubbles are formed on

or near the surface. b) Continued exposure leads to the formation of larger bubbles that

begin to coalesce and blister on the surface, with the help of irradiation-induced

diffusion dips, holes and other surface features begin to appear. c) Further irradiation of

these bubbles cause them to burst and create protrusions for finer nanostructures to

form, this d) Eventually leads to the fuzz nanostructure observed on tungsten at high

fluences [45].

2.2.4   Effect of helium Irradiation on retention properties of tungsten

Deuterium retention remains an important property for PFCs and many studies

have been conducted in regards to deuterium retention of PFCs after He irradiation

[32,47]. A study conducted by Nagata et al. [47] showed that helium pre-irradiation of

tungsten surfaces enhanced deuterium retention for surfaces at room temperature.

Figure 2.12 shows a significant increase in deuterium retention as a function of helium
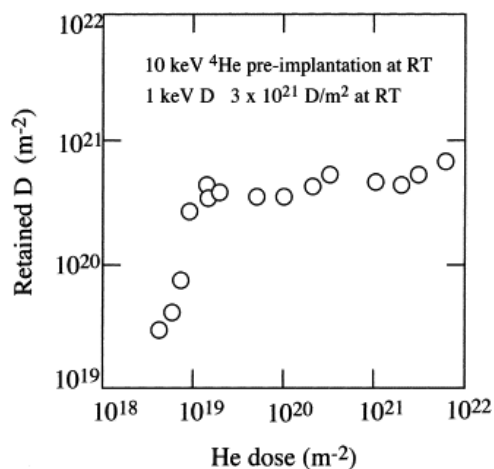
pre-irradiation.

Figure 2.12: Near surface retention of deuterium as a function of helium pre-irradiation fluence [47].

The Nagata et al. [47] study focused on high energy He irradiation up to 10 keV. Other

studies, like the one conducted by Ueda et al. [48], discuss the effect of helium

irradiation on deuterium trapping at lower energies. It appears that helium irradiation

reduces the diffusion length of the deuterium ions in the material. This causes increased

trapping near the surface at room temperature. As the temperature increases past

~500K, the retention of deuterium is greatly reduced due to the presence of helium [48].

2.2.5 Effect of helium irradiation on erosion

Another main area of interest regarding nanostructure formation on tungsten PFCs is

the erosion rates of the newly developed morphology. Erosion of the surface can have a

major impact on the plasma performance. Several studies have looked into the erosion

rate of fuzzy tungsten surfaces when exposed to He plasmas. One experiment

conducted by Y. Ueda et al. [48] looked a several different fuzz thicknesses that were

produced via 50 eV He ion irradiation with a flux of 1.0 x 10^{22} m^{-2}-s^{-1} at temperatures

ranging from 300 – 800 °C. The fuzz thickness on the different samples ranged from 300-

800 nm. These fuzzy surfaces were then exposed to a D-He plasma in the TEXTOR

machine and monitored for erosion [48]. Understanding the erosion rate of the

tungsten fuzz requires understanding of two competing effects. First, you have to take

into account the growth rate of the fuzz then the amount of material being eroded from

the wall. Ueda et al. reports that al the fuzz surfaces were either fully eroded or covered

by a carbon deposits due to the fact that TEXTOR is a carbon machine [48].

Another study by Tokitani et al. [49] also used a He ion irradiation in the linear

diverter simulator (NAGDIS) to grow a thick fuzz layer of 1.4 microns. This fuzz layer was

then exposed to the Large Helical Device (LHD). Exposure of the tungsten fuzz to 20 eV

hydrogen ions with a flux of ~10^{23} m^{-2}-s^{-1} caused large scale tungsten erosion. The cause

of this erosion is thought to be due to the high heat flux inducing unipolar arcing [49].

These results suggest that fuzzy surfaces could act as a tungsten source to the plasma

and have a detrimental effect on plasma performance.

Other studies, like the one conducted by Baldwin et al. [19], contend that the

newly formed nanostructure does not erode significantly under low energy ion

irradiation. In this work, 24 different tungsten samples were exposed to helium ion

energies between 25 and 65 eV and the temperature ranged from 900 to 1300 K. Mass

loss measurements were made after every exposure. Figure 2.13 shows the mass loss

data collected for each sample.
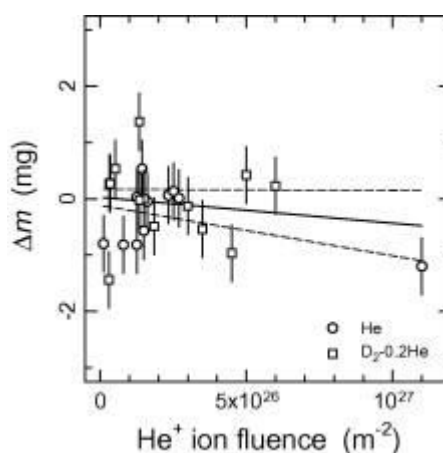
Figure 2.13: Mass change, Δm, on W targets following exposure to pure He or
D_2–0.2He mixture plasmas, plotted as a function of He^+ ion fluence received
during exposure[19].

This plot shows that there is not significant erosion of the tungsten surface due to low energy plasma bombardment. It is noted in the paper that this fuzz layer can be easily removed with light mechanical or abrasive action [19].

More research is needed to understand the relationship this new tungsten nanostructure will have with fusion plasmas. Currently, it seems that the nanostructure may be resistant to erosion via mechanisms like sputtering, but it may still undergo erosion from high thermal loads or abrasive action inside fusion devices.

2.2.6   Mechanical properties of ion-irradiated tungsten

A paper by James Gibson et al. [50] looks at the resulting changes in mechanical properties of tungsten after exposure to helium irradiation. In the experiment, tungsten samples were exposed to both a tungsten ion fluence of 5 x 10^{14} ion-cm^{-2} and helium ion fluence of 1.22 x 10^{16} ion-cm^{-2}. This was used to create three conditions to study; an unimplanted case, a tungsten ion only exposure, and a tungsten ion and helium ion exposure. Table 2.2 shows the effect that each case had on the mechanical properties of the tungsten samples.

Table 2.2: Comparison of modulus, yield stress and indentation hardness for the materials tested. One standard deviation of the scatter is given as an indication of the error in the results. The percentage increase above the unimplanted material is also shown [50].

	Irradiation condition		
	Unimplanted (7 cantilevers)	W ion (5 cantilevers)	W and He ion (8 cantilevers)
E (GPa)	418 ± 86	463 ± 34	496 ± 89
	0%	$10.8 \pm 2.4\%$	$18.8 \pm 5.2\%$
σ_y (GPa)	2.7 ± 0.4	3.0 ± 0.5	3.0 ± 1.2
	0%	$8.0 \pm 1.8\%$	$10.6 \pm 4.4\%$
Hardness (GPa)	7.15 ± 1.23	8.57 ± 0.76	9.1 ± 0.51
	0%	$19.9 \pm 4.1\%$	$27.3 \pm 5.2\%$

The results show an increase in hardness of 27.3% ± 5.2% from the unimplanted to the

W and He irradiated case. This shows an increase in hardness due to irraditiation.

2.2.7   Helium driven morphology evolution on various tungsten grades

The Baldwin et al.[19] paper looks at 9 different W and W alloy samples. All these

samples were exposed to pure He plasma for 1 hour at a temperature of 1120 K. The

cross-sectional SEM images of the exposed samples are seen in Figure 2.14. All of the

various W samples showed fuzz thicknesses of about 2-4 μm. The main exception was

the W sample that was prepared via powder metallurgy methods and then heat treated

to above recrystallization temperatures. The cross-sectional SEM image for this sample

showed fuzz thickness in excess of 7-8 μm [19]. In addition to fuzz thickness, these

micrographs show other interesting differences in morphology. This is highlighted most

noticeably in micrograph 2.14(f). In this cross-sectional image of the W- 1.5 % TiC

sample, there is substantial evidence of morphology changes even below the fuzz layer

[19].
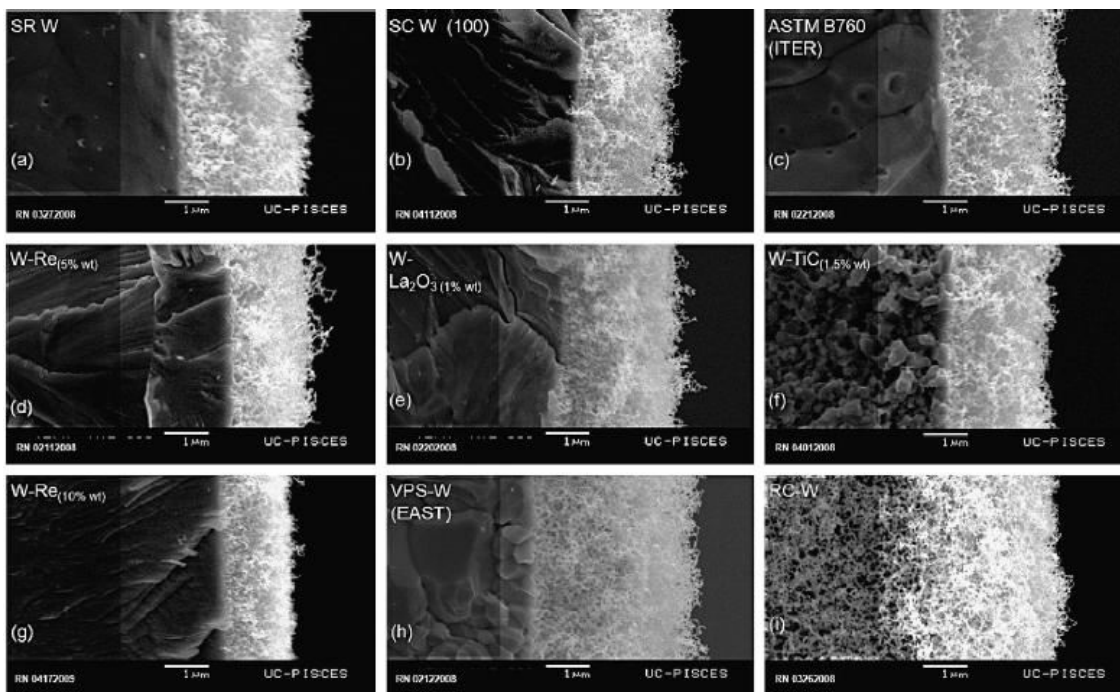
Figure 2.14: Cross-sectional SEM images for nine different grades of W relevant to fusion engineering practice. All target specimens were exposed to consistent pure He plasmas at 1120 K for 1 h. The He+ impact energy was 40 eV. The following grades are explored: (a) PLANSEE SR W, (b) SC h1 0 0i W, (c) ITER ASTM B760 compliant W, (d) PLANSEE W–Re (5% wt.), (e) PLANSEE W–La2O3 (1% wt.), (f) UFG W–TiC (1.5% wt.), (g) ULTRAMET CVD W–Re (10% wt.), (h) VPS W (EAST) and (i) W target produced by powder metallurgy methods but heat treated to above the recrystallization (RC) temperature(1800 K) [19].

Due to the extreme difference in the recrystallized sample's response to the

irradiation environment, further SEM analysis was conducted on other regions of the

sample. This investigation revealed that there was evidence of microstructure alteration

as deep as 300 µm [19]. This large deviation in behavior is conjectured to be related to

the recrystallization process that the sample was subjected to. The basic premise is that

recrystallization leads to a net flux of defects to the grain boundaries. This is driven by

the high temperature inducing higher diffusion rates. The large increase in defects at the

boundary act as trapping sties for He. Thus, there is more bubble growth, which then

drives this microstructure formation [19]. The results from this study did not reveal an

effective material design method to prevent fuzz formation on these different tungsten

materials. Another study by Kajita et al. [36] looked at undersized atom doped tungsten

alloys. These materials responded similarly to the pure tungsten samples, implying that

undersized atoms may not have a role in suppressing nanostructure formation [36].

Despite these setbacks, continued research is being conducted in designing materials

that are resistant to the extreme morphology changes induced by helium irradiation.

2.3   Chapter Summary

Tungsten undergoes a wide range of changes when exposed to both helium and

deuterium plasmas. In the case of deuterium, the formation of bubbles and blisters are

evident provided that the ion energy is above ~23 eV and temperatures below 700 K.

This temperature threshold seems to be connected to a similar drop in deuterium

retention that is observed past 700 K. This implies that the formation of bubbles and

blisters play a key role in the retention mechanisms of deuterium in tungsten.

A similar story is seen when exposing tungsten surfaces to fusion-relevant

helium plasmas. However, rather than seeing bubble formation suppressed beyond

temperatures of 700 K, it is observed that bubble formation and coalescence is increased. This bubble formation is then followed by the development of a fuzzy nanostructure on the surface. A lot of research has been conducted in order to investigate the driving mechanisms behind this new morphology and the subsequent effects it will have on the plasma performance of fusion devices. Research shows that fuzz formation requires temperatures above ~873 K and helium ion energies above ~20-25 eV. Helium irradiation of tungsten has been shown to increase deuterium retention and hardness of the material. Erosion of the nanostructure is still being investigated. The potential problems that this new surface morphology presents have prompted new research in designing new PFCs that are resistant to this nanostructure formation.

The subject of investigating the mechanisms which cause this morphology change lead to the focus of this thesis. In some previous studies it was shown that higher grain boundary density can lead to a reduction in radiation damage. This specific question on grain size is explored further in subsequent chapters.

CHAPTER 3.   EXPERIMENTAL FACILITIES

The testing of candidate materials for use in fusion devices is not easily

accomplished. It requires either a full fledged fusion reactor or some substitute machine

that is capable of reproducing the desired conditions. The first case may seem like the

clear best option, but in reality the tests are limited by the machine itself and getting

the desired diagnostics to perform surface analysis studies may be impossible. These

issues may include how often you can replace samples and what diagnostics can be used

in between plasma shots in the device. An example of an issue with using a fusion

machine to study surface evolution can be seen from work presented by Allain et al. [51].

This work discusses the use of lithiated ATJ graphite tiles that were exposed to plasma

for an entire campaign (these can be months long) in the National Spherical Torus

Experiment (NSTX) reactor at Princeton Plasma Physics Laboratory. Due to the constant

operation of the NSTX machine, data points can only be taken from the beginning and

end of the campaign. This can result in missing key steps in the evolution of the surface.

This issue prompted the ongoing development of the Materials Analysis and Particle

Probe (MAPP). This is a device that can be attached to NSTX to insert and retract

different material samples into and out of NSTX to perform *in-situ* surface diagnostics in

between plasma shots of the NSTX reactor [52].

An alternative to testing materials in fusion devices is the use of linear plasma devices. These are generally large vacuum chambers equipped with a plasma source that can generate a plasma with parameters that are relevant to fusion conditions. There are several advantages to testing materials in a linear plasma device. First, they are easier to get access to. Second, it is easier to control and monitor the key parameters at the surface of the sample. This is in large part due to the design of these types of machines. For example, most linear plasma devices were designed specifically to test how different materials respond to high flux plasma sources. However, it is impossible to recreate a true fusion environment in these sources, which makes the study of competing mechanisms or studies about neutron irradiation nearly impossible. However, the reduction in the complexity of the system is ideal for fundamental studies and isolating certain mechanisms of interest. This makes the use of linear plasma devices ideal for the study of new candidate fusion materials.

3.1   Major Linear Plasma Devices

There are many major linear plasma devices that are in operation around the world, but the three that will be presented here are chosen because of their work in regards to fusion PFCs. PISCES-B linear plasma device located at the University of California San Diego, in the United States, NAGDIS-I and NAGDIS-II located at the OHNO lab in Nagoya University in Japan, and the Nano/Pilot/Magnum - PSI devices located at the Dutch

Institute for Fundamental Energy Research (DIFFER) in the Netherlands are all high flux

devices aimed at understanding plasma material interaction.

The PISCES-B facility is capable of creating a wide range of plasma conditions.

Table 3.1 is a concise summary of the facility's parameter space.

Table 3.1: Experimental conditions in PISCES-B facility. Table taken from Hirooka et al. [53].

Parameters	Achievable
Plasma species	H, D, He, Ar, N
Pulse duration (s)	Continuous
Plasma density (cm^{-3})	up to 3×10^{13} (D)
Electron temperature (eV)	5–30
Ion bombarding flux $(ions/cm^2/s)$	up to 3×10^{19}
Ion bombarding energy (eV)	30–500 (d.c. bias)
Surface temperature (°C)	R.T.-1600

In addition to the stated parameter space, PISCES-B is in a clean room that is designed

to deal with beryllium materials for fusion applications. This is a major focus of the

plasma material interaction research being done there. There is also a considerable

amount of work being done on tungsten fuzz nanostructure formation, being led by M. J.

Baldwin and R.P. Doerner. Some of their results have already been discussed in previous

chapters.

The NAGDIS-I and NAGDIS-II facilities are another example of a linear plasma

system, but the focus of these devices is more specifically geared towards material

analysis in the divertor region of fusion devices. Figure 3.1 is a schematic of what the device looks like.
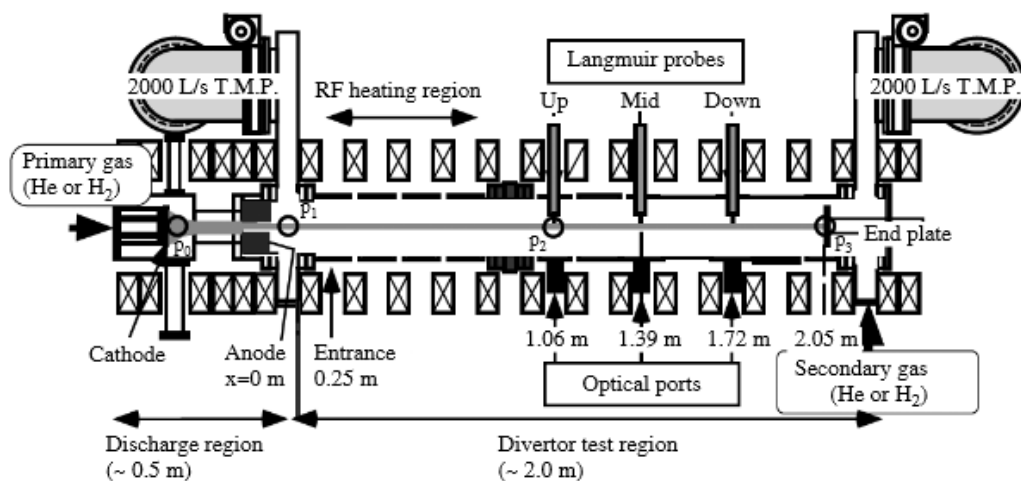
Figure 3.1: This is a schematic of the NAGDIS-II machine at Nagoya University[54].

The plasma is created from a high density plasma source, which uses LaB_6 disk for a cathode, an intermediate hollow SUS electrode, and a hollow copper anode [54]. This source keeps the discharge voltage less than 100 V for helium and less than 200 V for hydrogen. Due to the ionization efficiency, a high gas pressure is needed in the source to generate dense plasma. This is compensated at the sample by use of differential pumping [54]. There are also 21 solenoidal magnetic coils that generate a magnetic field strength up to 0.25 Tesla, which is used to increase plasma density. This facility can simulate high temperature plasma exposures similar to divertor conditions in future fusion devices. This machine has been used for a lot of studies regarding helium irradiations on tungsten. Select data from these studies has been discussed in chapter 2.

The final facility to highlight is the PSI machines at DIFFER. DIFFER has the use of three separate machines that are all similar but have key differences that can be utilized depending on the intended research. All the machines use a cascade arc plasma source design [55]. The basic set up of this source is an anode, a stack of electrically isolated plates, and three cathodes [56]. The cathodes are made from a sharp thoriated tungsten pins that are 1-2 mm in diameter, depending on current used. Current through the tip causes electron emission, which ionizes gas that has been is fed into the source [56]. The plasma arc is fed along the arc channel, which is created by the stacked and isolated copper plates with bores in the center. This plasma will expand supersonically into the vacuum system [56]. A more detailed description of this design is explained by Kroesen et al. [56]. The main difference between the PSI machines is what can be done to the plasma after it leaves the arc cascade source.

The smallest machine is the nano-PSI machine. This device has no magnetic coils to produce a magnetic field to focus the plasma. As a result, the flux at the surface of the sample exposed in this machine is low (~1 x 10^{20} ions-m^{-2}-s^{-1}). This lower flux means that the sample is not heated by the incident ions. This is an advantage, because it allows for very accurate temperature control of the sample using a stage heater. The lower flux is also better for conducting low fluence studies.

The next device is the Pilot-PSI device. This device has the addition of magnetic field coils to produce a magnetic field up to 1.6 Tesla. This enables the device to produce fluxes on the order of (~1 x 10^{24} ions-m^{-2}-s^{-1}) [55]. The huge increase in ion flux results in heating of the sample surface. This is compensated by the use of a water cooling stage.

However, it is much harder to get precise temperatures for exposure, since the heating of the sample is linked to the plasma parameters like ion energy, flux, thermal contact of the sample to the cooling plate etc. Surface temperature monitoring is done using a fast infrared camera (FLIR SC7500MB) camera, which is validated using a pyrometer. Making use of the ion induced heating and the water cooling, it is possible to maintain temperatures reliably between ~600 -1800 °C with adjustment of the plasma parameters. This machine is ideal for getting high fluence exposures with a variety of interrogating species (Ar, He, D etc.)[57]. In addition to doing steady state plamsa exposures, Pilot-PSI can run a pulsed plasma source during steady state irradiations to simulate ELMs in tokamaks. This allows observation of how materials respond to high frequency increases in heat flux.

The Pilot-PSI acted as a validation for DIFFER to build their final machine, Magnum-PSI. This machine is essentially an upgraded version of the Pilot-PSI machine with several key upgrades. It has a better sample mounting system to mounts samples ranging from small 1 cm^2 disks to diverter plates. It also is equipped with a better pulsed plasma system which can pulse at 10 Hz and reach peak heat fluxes of 1 GW-m^{-2} [58]. Below is a table that summarizes the capabilities of these different linear plasma devices and directly compares them to the conditions expected in DEMO.

Table 3.2: Relevant parameters of linear divertor plasma simulators compared to the expected operating conditions of the DEMO reactor. Image provided by Greg De Temmerman.

			Linear Divertor Plasma Simulators					Reactor
		PISCES-B	NAGDIS-II	PISCES-A / TPE*	PSI-II	PILOT	MAGNUM	DEMO
Discharge		Refl. Arc	Pen.	Refl. Arc	Pen.	Arc Casc.	Arc Casc.	Divertor
Power	(kW)	5–15	10.5	5–10	6.5	45	270	
p_{target}	(Pa)	0.01–1	0.1–4	0.01–1	0.01–0.1	1–10	< 10	
T_i	(eV)	10–300	50	10–200	< 15	0.1–5	0.1–10	<100
T_e	(eV)	3–50	10	3–20	< 30	0.1–5	0.1–10	< 100
n	(m^{-3})	10^{17}–$2\cdot10^{19}$	$6\cdot10^{19}$	10^{17}–10^{19}	10^{19}	$4\cdot10^{21}$	10^{20}	~ 10^{20}
Ion flux	(m^{-2}s^{-1})	10^{21}–$2\cdot10^{23}$	10^{22}	10^{21}–$3\cdot10^{22}$	10^{22}	$5\cdot10^{24}$	10^{24}	10^{23}–10^{24}
Energy flux	(MW·m^{-2})	1–10	0.01	2	0.1	30	10	10
B	(T)	0.04	0.25	0.1	0.1	1.6	3	10
Beam dia.	(cm)	5	2	5	6–15	1.5	10	
Length		1.5	2.8	1	2.5	0.5–1		
Heating	(kW)	< 3 dc	~50 rf	< 1 dc	5	10 dc	50 dc + rf	Thermal
				PMI capabilities				
Gas species		D, He	D, He	D, T*, He	D, He	D, He	D, He	D, T, He
Targets		Be, C, W	W, C	Be*, W, C	W, C	W, C	W, C	W
Pulse length	(s)	steady	steady	steady	steady	10	steady	steady
Impurity PMI		Be, C						W
Transients		YAG	YAG					ELM Neutron
Damage Fluence (/ day)	(m^{-2})	~10^{27}	~10^{26}	~10^{26}	~10^{26}	~10^{26}	~10^{28}	>10^{28}

In service | Not operational | Near condition | Meets condition | Below condition

Due to the versatility and the range of experiments that can be done at DIFFER. ehe bulk of the irradiation work presented in this thesis was done at the DIFFER facility. Using the low flux device combined with the high flux exposures, it was possible to map out the parameter space for our ultrafine grained tungsten samples. The Magnum-PSI also may play a key role in future investigations to grain size behavior during transient plasma exposures.

3.2   *In-Situ* TEM facility

To complement the experiments being conducted at DIFFER, the use of an *In-situ* TEM facility was coordinated to provide some real time insight to the damage process that tungsten samples undergo when exposed to helium plasmas. The Microscope and Ion Accelerator for Materials Investigation (MIAMI) facility was an ideal lab to examine the ultrafine grained samples under real time helium irradiation. The facility is capable of irradiating with most ion species, with energies between 2 - 100 keV, and with fluxes between 10^{14}-10^{18} ion-cm^{-2}-s^{-2} [59]. This can all be done while performing *In-situ* TEM with a JEOL 2000FX TEM. This facility allows for direct observation of defect and damage behavior during the early stages of tungsten irradiation.

CHAPTER 4.   THE EFFECT OF GRAIN SIZE ON HELIUM INDUCED MORPHOLOGY
EVOLUTION IN TUNGSTEN

Extensive research is being conducted to discover ways to reduce irradiation damage in tungsten when exposed to high temperature, high flux helium irradiation. These are the types of conditions that are expected in future fusion devices. Several promising avenues of research have surfaced, ranging from application of low Z films on tungsten [60,61] to various composites and tungsten alloys [62, 19]. Another promising method to produce radiation resistant materials is the formation of ultrafine and nanocrystalline grains. These are grains that are less than 500 nm (ultrafine) and 100 nm (nanocrystalline) in size [63,64].

A paper by Bai et al. [65] discussed the role of grain boundaries on irradiation tolerance. Specifically, materials with smaller grains will consequently have a higher grain boundary density. Grain boundaries have been shown to absorb interstitials formed during irradiation-induced collision cascades. These interstitials can then be emitted from the grain boundary to combine with vacancies within the grain [65]. This reduces the trapping of helium within the grain itself. Grain boundaries themselves are also strong traps for helium atoms and other defects [66,67,68]. The result is that a higher proportion of the damage-induced defects linked with tungsten morphology evolution migrate to the brain boundaries instead of remaining in the grains themselves.

Further research specifically focused on the role of grain size on radiation tolerance is presented in this chapter.

4.1   Tungsten of different grain sizes

To investigate the role that grain size plays in the irradiation tolerance of tungsten, three different samples were used. Commercial samples are standard pure tungsten with an average grain size of ~1-5 µm.

The next type of sample investigated is multi-modal tungsten (MMW). MMW samples are made using a process known as Spark Plasma Sintering (SPS). This process sinters tungsten powders (~ 1µm) to create a tungsten material with multi-modal grain size distributions. Both consolidating the tungsten powders at temperatures between 1300 – 1400 °C and pressures between 90-266 MPa inhibit grain growth [69]. The smaller grains increase the hardness of the sample, while the larger grains are thought to make the sample more ductile [69]. Figure 4.1 is an SEM image of what the MMW morphology looks like prior to irradiation. As we can see, there is a multimodal distribution of grain size. The larger grains are several microns on average and the small grains are ~500 nm on average. These samples are formed into 1 cm^2 disks that are roughly 4 mm thick.
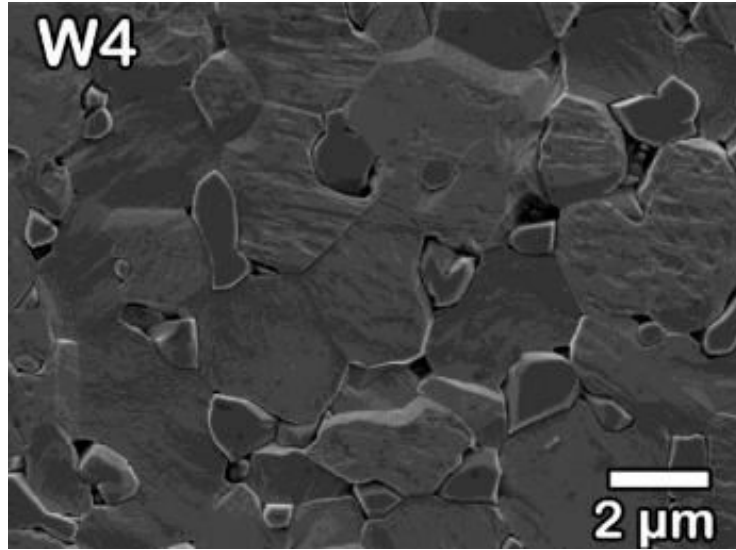
Figure 4.1: This image is a SEM image taken of one of the MMW samples. From this image the multi-model grain distribution is readily seen [69].

The last type of tungsten sample studied is severe plastic deformation (SPD) samples. SPD samples are made by controlling the thermo-mechanical conditions during the deformation of the surface of commercial tungsten. A wedge is used to cut a preset thickness from a commercial tungsten disc by applying a large shear strain to a narrow deformation zone. A more detailed explanation of this machining method is discussed in Efe et al. [70]. The result of this creates a tungsten surface with average grain sizes 300 - 100nm [70]. Figure 4.2 is a TEM image of the microstructure of a SPD sample prior to irradiation. As seen in the image, SPD samples have long narrow grains that are formed as a result of the machining process.
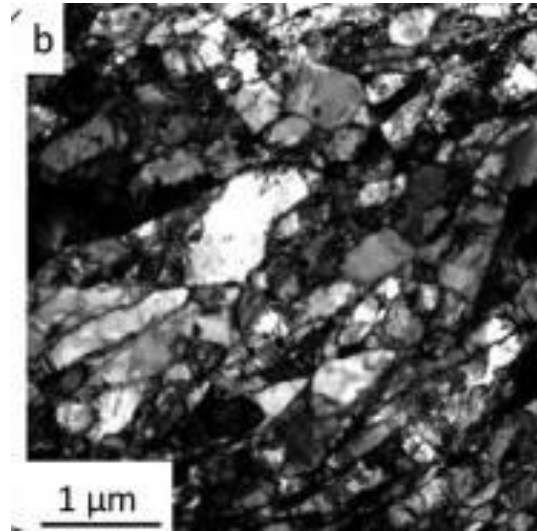
Figure 4.2: This image is a TEM image taken of one of the SPD samples. From this image it is clear to see the formation of very small grains [70].

The long narrow grains are classified as ultra-fine or nanocrystalline based on the thickness of the grains' smallest dimension. This better represents the shortest distance implanted helium must travel to reach a grain boundary. As reported earlier by Bai et al. [65], the key to radiation tolerance is the likelihood that interstitials and vacancies can recombine and reduce the trapping of helium within the grain. Post machining of the tungsten creates thin, slightly curved samples which are about 400 microns thick and ~5 mm x 4 mm in size.

The three types of tungsten samples presented here have been exposed to a large range of plasma conditions and their responses have been detailed in the following sections.

4.2   Experimental Methods

All tungsten samples were mechanically polished using lapping films to a mirror finish before exposure in the DIFFER devices. Once polished, samples were mounted one at a time into the desired machine. For the nano-PSI machine, this simply meant placing the tungsten sample on a stage heater with the polished side facing up. Once placed, the nano-PSI vacuum chamber was pumped down to mTorr pressures before starting the heater. Once the heater reached the desired temperature, the ion source was turned on. The flux at the surface was monitored using a Thompson scattering laser system and the ion energy at the surface was set by applying a bias to the sample. For the low fluence study done at DIFFER, two ion energies were used (30 eV and 70eV) and three different temperatures (300, 600, and 900 °C) were used to irradiate 6 different SPD tungsten samples to ~1×10^{23} ions m^{-2} . In addition to these SPD samples five more SPD samples were irradiated to different fluences ranging from ~5×10^{20} - 1×10^{24} ions-m^{-2} at 30 eV and 900 °C. After the desired fluence was achieved, the sample was allowed to cool in the chamber before the vacuum was broken to prevent oxidation of the heater. These samples were then shipped back to Purdue University for post-irradiation analysis using Scanning Electron Microscopy (SEM) and Focused Ion Beam microscopy (FIB).

For the high fluence work, polished commercial, MMW, and SPD tungsten samples were mounted in the Pilot-PSI device. This required the use of a clamping ring which pressed the samples against the cooling plate inside the Pilot-PSI chamber. This

was straightforward for the commercial and MMW samples because of their standard 1

cm^2 disk shape. The SPD samples were more difficult, as their slightly bent and irregular

shape required the samples to be mounted by slipping the edge of one side of the

sample under the clamping ring and then carefully tightening the mount to avoid

cracking the sample down the middle. Once mounted, the system was pumped down

before starting the plasma source. Once the source was ignited, the magnetic field was

brought to 1.6 Tesla in order to focus the plasma and achieve the high flux required to

investigate the high fluence parameter space. The range for the parameters in Pilot-PSI

device were helium ion fluxes of ~1.0×10^{23} – 2.0×10^{24} ions m^{-2} s^{-1}, helium fluences of

~1.89×10^{25} – 1.01×10^{27} ions m^{-2}, sample temperature ranges from ~600 – 1500 °C and

helium ion energy from 30-65 eV. A more detailed description of each sample's

experimental conditions can be found in the high fluence studies section in Table 4.1.

As in nano-PSI, the flux was recorded using a Thompson scattering laser system. The

variation in the ion energy was primarily used to control the temperature of the sample.

This was due to the observation that varying the ion energy seemed to have little impact

on the observed morphology changes due to irradiation. Temperature has been shown

to be a much more important parameter to keep controlled. Monitoring of the

temperature was done with a fast infrared camera (FLIR SC7500MB) camera, which is

validated using a pyrometer. In the cases presented here, this gave reliable average

temperatures with an error of ± 50 °C. After the sample had reached its desired

exposure, the plasma source was turned off, the sample was allowed to cool, and then it

was removed from the chamber. These samples were then shipped back to Purdue

University for post-irradiation analysis using Scanning Electron Microscopy (SEM) and Focused Ion Beam microscopy (FIB).

For the SPD tungsten TEM samples that were used for the *In-situ* TEM experiments conducted at the MIAMI facility, special sample preparation was needed. Mechanical polishing was conducted to both sides of a 400 μm thick standard SPD sample. Once the sample had been polished down to a thickness of 100 μm, it was taken to an electropolishing machine located in the Neil Armstrong Hall of engineering at Purdue. The electropolishing solution used was a 0.1 wt-% NaOH solution. In this process, the electrolyte solution acts as an anode and is in contact to the positive terminal of a DC power supply. The SPD sample is connected to the cathode. Applying a DC voltage to the sample causes it to oxidize and the oxidized material is removed by the electrolyte solution. This process is continuous and only stops when a light sensor determines that the sample on the cathode reaches a desired TEM sample thickness. During analysis of the TEM samples, no significant difference in mass-thickness contrast was observed. This indicates that the samples were evenly etched.

These TEM samples were shipped to MIAMI facility at the University of Huddersfield. This facility conducted the *In-situ* TEM experiments. SPD TEM samples were exposed to a 2 keV helium ion source with a flux of $3.3{\times}10^{16}$ ions.m^{-2} -s^{-1} at 950 °C. This was done while simultaneously looking at the sample with the JEOL JEM-2000FX TEM. Heating control was achieved with a Gatan Model 652 heating holder, and TEM imaging recording was captured using a Gatan ORIUS SC200 digital camera [59].

The camera recorded 480 x 480 pixel images at a rate of 8 Hz. All images were taken in bright-field TEM condition ± 1.5 μm of defocus.

Additional SEM and FIB analysis was performed at the Birck Nanotechnology Center at Purdue University. The use of the FEI Nova 200 NanoLab DualBeamTM-SEM/FIB machine was used to make cuts into the pre-irradiated tungsten samples sent back from DIFFER. This machine uses Ga ions to etch small regions into the sample. This allowed for top view SEM images of the changed surface morphology, as well as cross-sectional SEM images to give depth information on the damaged region.

4.3   Low fluence studies at DIFFER

Before launching into the high fluence work, some initial low fluence studies were conducted on the SPD tungsten samples. The focus of these experiments was to gain some insight to the early stages of tungsten morphology evolution. Samples discussed in this section were exposed in the nano-PSI device located at DIFFER. As mentioned earlier, this device uses a cascade source [73] to produce ion fluxes of $\sim 10^{20}$ ions m^{-2} s^{-1} at the sample surface. Sample temperature is controlled be a heating stage up to 900 °C. Figure 4.3 shows 6 SPD samples exposed to helium plasma to a fluence of $\sim 1 \times 10^{23}$ ions m^{-2} at various temperatures.
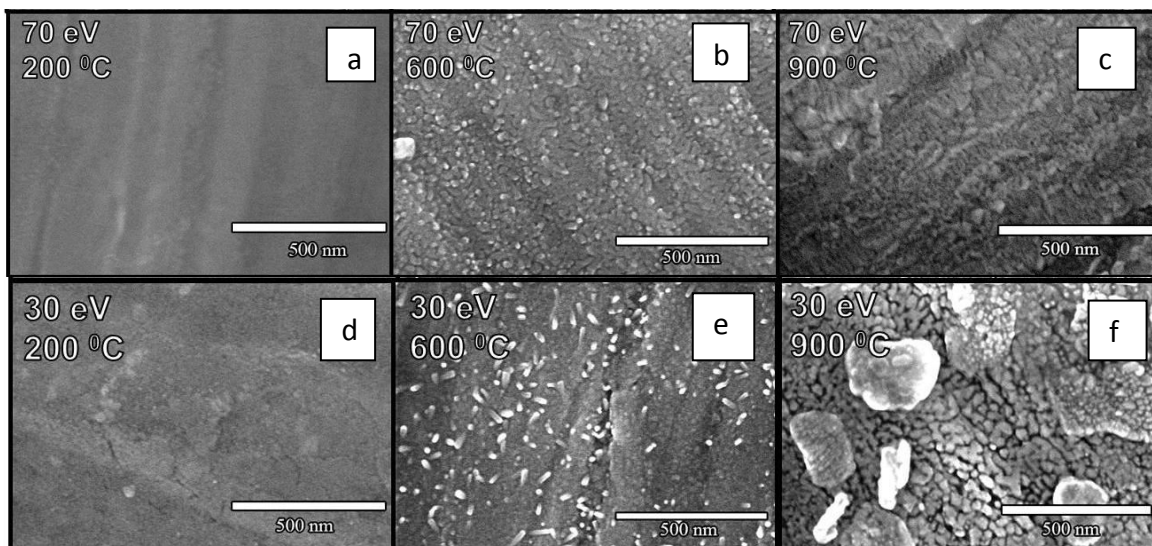
Figure 4.3: These are 6 SEM images of SPD samples exposed to 30 eV or 70 eV helium plasma until a fluence of ~1 x 10^{23} ions m^{-2}. The main difference in the exposures is temperature which increases from right to left.

From figure 4.3, there is a clear connection between the temperature and the damage on the surface. This is consistent with what is seen in literature regarding commercial tungsten. The 200 °C case exhibits very little morphology change while the 900 °C case is becoming porous. It is important to note that the ion energies are well below the displacement energy for helium on tungsten. There is not a significant difference between the 30 eV cases and the 70 eV cases, either. This is not surprising, as both energies are past the minimum energy to observe fuzz growth in high fluence exposures but are still below the displacement energy for helium on tungsten, as mentioned earlier. This implies the damage is being driven by other mechanisms. Some suggested mechanisms to support these observations are loop punching [71] and irradiation enhanced surface diffusion [72]. Another key observation from these samples is the

observation of damage despite the low flux and fluence. This is important, as the flux

threshold for nanosturucture formation is much higher than the flux used for these

samples.

The lead up to the high fluence work is characterized by figure 4.4, which shows

SPD samples irradiated at 30 eV, 900 °C to various fluences. This figure provides some

insight as to the rate at which damage is occurring in the SPD tungsten materials.
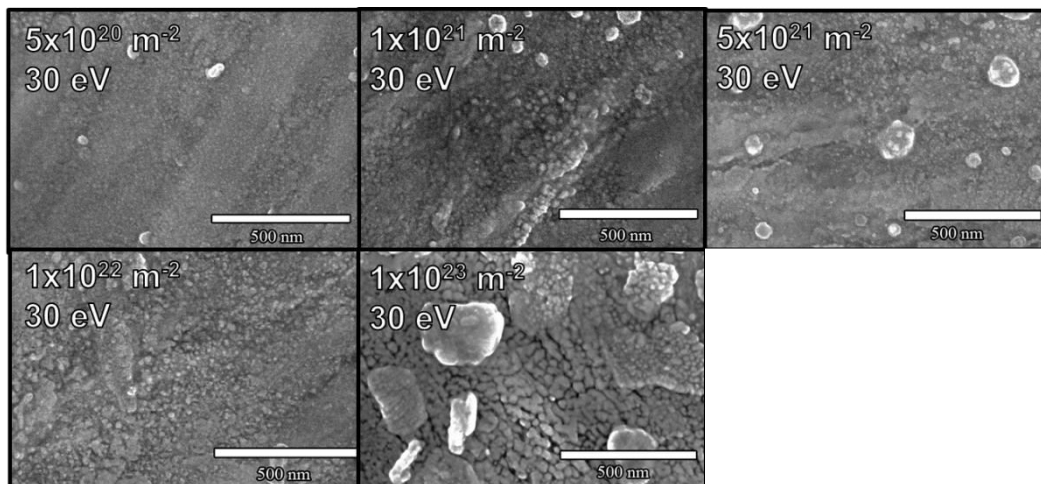
Figure 4.4: These are 5 SPD sample all exposed to 30 eV helium irradiations at 900 °C to fluences between 5×10^{20} - 1×10^{24} ions m^{-2}.

Figure 4.4 shows that there is some roughening and pitting that is beginning to occur

near the 1×10^{23} ions m^{-2} stage, but there is not significant damage compared to what is

observed in the high fluence cases.

In-Situ TEM of low fluence helium exposures is discussed in a later section. The

need to understand the early stage process is key in discovering the mechanisms that

produce extreme changes in surface morphology at high fluences. Subsequent high

fluence exposures are presented later to connect the early stage change to the final microstructure.

4.4 High fluence studies at DIFFER

This section details the work conducted at DIFFER regarding the exposure of tungsten samples with varying grain size to high flux, high fluence, low energy helium irradiation in the Pilot-PSI linear plasma device. This is a high-flux machine capable of reproducing fusion-like conditions. This system uses a cascade arc source [73] that discharges into a vacuum chamber [74]. Along the chamber, there are five coils that produce a pulsed axial magnetic field up to 1.6 tesla. The discharged plasma is focused by the magnetic field and directed towards a water cooled target. This system was used to achieve helium particle fluxes of ~1.0×10^{23} – 2.0×10^{24} ions m^{-2} s^{-1}, sample temperature ranges from ~600 – 1500 °C and helium ion energy from 30-65 eV. The temperature of the sample was recorded using a pyrometer and validated by an IR camera focused on the sample surface. The flux at the sample was calculated by using a Thomson Scattering system 17 mm in front of the target [73].

Post-irradiation, the samples were shipped back Purdue University, and SEM and FIB analysis was conducted at Birck Nanotechnology center. Cross-sectional images were taken using focused ion beam analysis. Table 4.1 is a summary of all the samples exposed in Pilot-PSI that are presented here as part of the high fluence work.

Table 4.1; Summary of irradiation parameter space for high-flux plasma exposures in Pilot-PSI experiments. Incident particle energy established by sample bias.

Sample	Sample Bias (V)	Flux (ions cm^{-2}s^{-1})	Fluence (ions cm^{-2})	Temperature (°C ± 50 °C)	Morphology
SPD 1	-30	1.00E+20	1.00E+22	~650	No fuzz, but porous
SPD 2	-40	6.00E+19	1.89E+21	900	No fuzz, but some roughness due to irradiation damage
SPD 3	-50	4.64E+19	1.03E+22	900	More damage and the beginning of hole and tendril formation
SPD 4	-40	6.63E+19	4.57E+22	933	Fully developed fuzz about 1 micron thick
SPD 5	-40	6.00E+19	1.01E+23	900	Fully developed fuzz about 3-4 microns thick
SPD 6	-40	6.00E+19	9.93E+21	1200	Intermediate stage before fully developed fuzz, pores and ridges have formed
SPD 7	-65	8.70E+19	1.00E+22	1503	Fully developed fuzz about 1 micron thick
SPD 8	-40	6.63E+19	4.57E+22	933	Fully developed fuzz about 1 micron thick
SPD 9	-60	3.22E+19	6.02E+22	902	Fully developed fuzz about 2-3 microns thick
MMW	-50	7.00E+18	6.43E+21	900	Nearly fully developed Fuzz < 1 micron thick

The first SPD sample that is presented (SPD 1) was irradiated at ~650 C with 30 eV helium ions. The flux of the helium ions was 1.00 x 10^{24} ions-m^{-2}s^{-1} and the fluence

that the sample was exposed to was 1.00 x 10^{26} ions-m^{-2}. Figure 4.5 shows an SEM image of the sample surface.
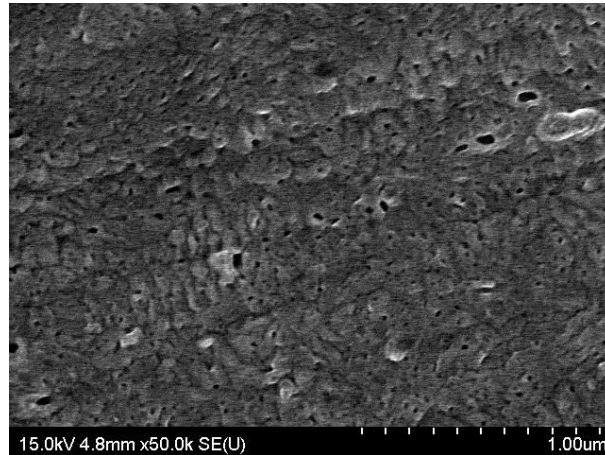
Figure 4.5: This is an SEM image of SPD 1 exposed to 30 eV helium plasma. The surface temperature during irradiation was ~650 C and the flux and fluence were 1.00 x 10^{24} ions-m^{-2}s^{-1} and 1.00 x 10^{26} ions-m^{-2} respectively.

As seen in figure 4.5, no tendril nanostructure has begun to form. There is evidence of irradiation damage and the surface has started to form pores. The low temperature is likely suppressing bubble formation, as interstitial and vacancy migration is limited. However, looking at some SPD samples exposed to similar fluxes and fluences at a slightly higher temperature, more significant damage is observed. Figure 4.6 shows four different SPD samples (SPD 2-5) all exposed to helium irradiation at 900 °C.
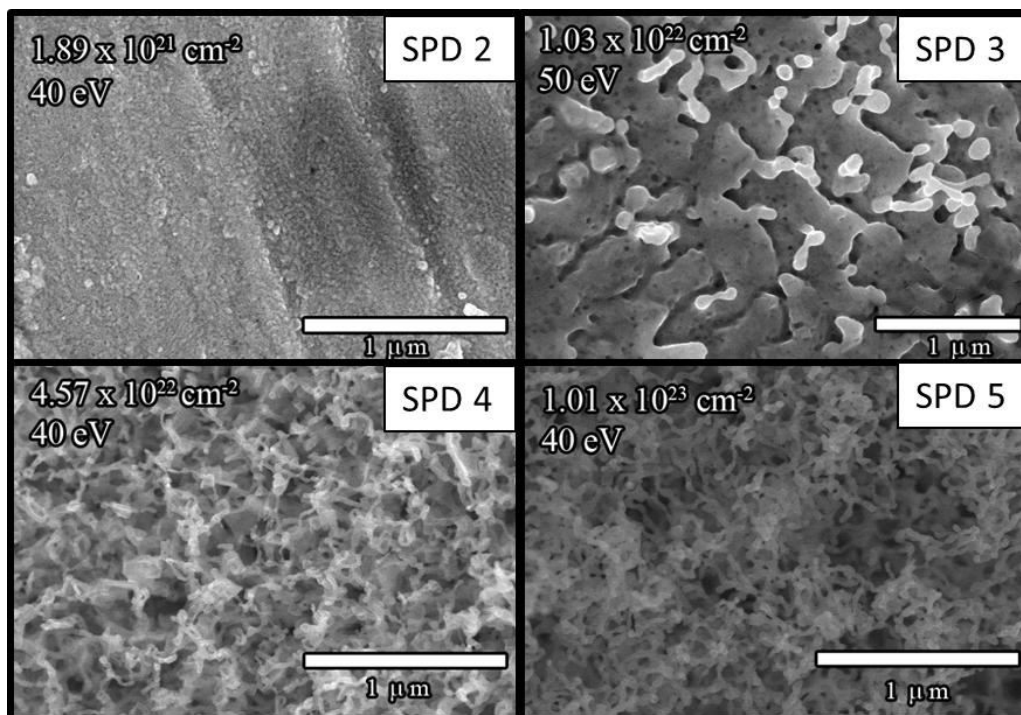
Figure 4.6: This shows SEM images of SPD 2-5 all exposed to helium plasma at 900 C [75].

These four images show the progression of the fuzz nanostructure as a function of increasing fluence. At a fluence of 1.8 x 10^{21} cm^{-2}, surface roughening has occurred and the formation of small pores appears to have started. At 1.0 x 10^{22} cm^{-2}, the pores are much larger and the surface has some tendril-like bases beginning to form. At 10^{23} cm^{-2}, fully developed fuzz has formed. These samples differ from SPD 1 primarily in that they were exposed at a higher temperature. There is some fluctuation in the ion energy, but ion energy was shown to not have a major effect on the irradiation damage, provided the ion energy is above the threshold energy for damage in tungsten. This is estimated to be ~27 eV by DeTemmerman et al. [76]. At 900 °C the vacancy and interstitial migration are more likely. This allows for the formation of large bubble which

is suspected to be one of the driving forces behind fuzz formation. This temperature threshold for nanostructure formation is consistent with the work published by Kajita et al. [18] shown in figure 2.10.

The main difference observed in the SPD samples when comparing them to commercial samples exposed to similar conditions is the fluence threshold at which fuzz is observed. Figure 4.7 compares fuzz thickness formed on commercial samples vs. SPD samples under similar conditions.
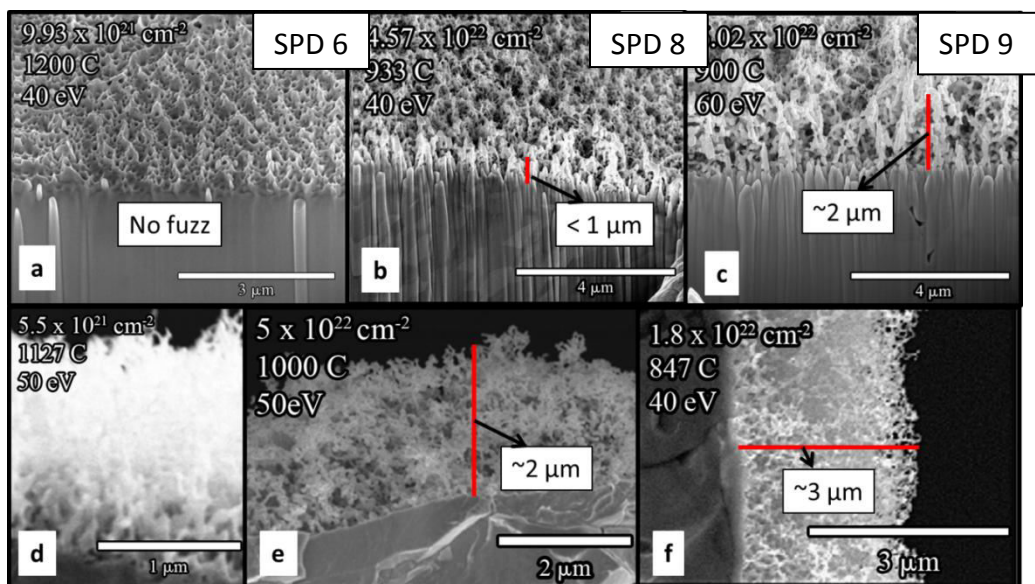
Figure 4.7: Cross-sectional SEM images comparing SPD tungsten samples to coarse-grained tungsten samples exposed to similar conditions. **(a)** SPD 6 irradiated in Pilot-PSI up to a fluence of 10^{22} cm^{-2} and 40 eV energy and temperature of 1200 °C, **(b)** SPD 8 irradiated in Pilot-PSI up to a fluence of 4.7x10^{22} cm^{-2} and 40 eV energy and temperature of 933 °C, **(c)** SPD 9 irradiated in Pilot-PSI up to a fluence of 6x10^{22} cm^{-2} and 60 eV energy and temperature of 900 °C. **(d)** Cross-sectional SEM image taken from Kajita et al. [18], Figure 2(e) with conditions: fluence of 5.5 x 10^{21} cm^{-2}, temperature 1127 °C, and ion impact energy of 50 eV. **(e)** Cross-sectional SEM image taken from Ueda et al. [32], Figure 4 (lower right) with conditions: fluence 5 x 10^{22} cm^{-2}, temperature of 1000 °C, and ion impact energy of 50 eV. **(f)** Cross-sectional SEM image taken from Baldwin et al. [19], Figure 5(c) with conditions: fluence of 1.8 x 10^{22} cm^{-2}, temperature of 847 °C, and ion impact energy of 40eV. The SEM cross-sectional images of SPD samples used a tilt angle of 52 degrees. Therefore, direct comparison is not possible; nevertheless, one can approximate the thickness and phase morphology from the images [75].

Figure 4.7 shows SPD samples (6,8,9) directly compared with commercial tungsten samples from the Kajita et al. [18], Ueda et al. [32] and Baldwin et al. [19] studies. Figure 4.7(a) (SPD) and 4.7(d) (commercial) are cross-sectional SEM images of tungsten samples exposed to similar conditions. The SPD sample has developed large pores and the surface has started roughen considerably; however, the commercial sample already shows ~2 microns of fuzz. It is important to note that no fully formed fuzz is seen in figure 4.7(a) despite the fact that the SPD sample has been exposed to almost twice the fluence of the commercial sample. Comparing 4.7(b) (SPD) and 4.7(e) (commercial), a similar observation can be made. The SPD sample has less than a micron of fuzz, while the commercial sample has nearly 2 microns for samples exposed to nearly the same fluence. This trend continues with figure 4.7(c) (SPD) and figure 4.7(f) (commercial), with the SPD sample having less fuzz despite being subjected to three times the fluence of the commercial sample. The data reported in literature by Kajita et al. [18], Ueda et al. [3232], De Temmerman et al. [76], and Baldwin et al. [19], all show commercial tungsten samples with fuzz formation occurring around ~5 x 10^{21} cm^{-2}. The SPD tungsten samples were still not showing fuzz formation after fluences into the 10^{22} cm^{-2} range. This implies that the fluence for fuzz formation in SPD tungsten materials is approximately an order of magnitude higher than in commercial tungsten samples.

Another interesting observation was made regarding the fuzz formation process in these SPD tungsten samples regarding temperature. Figure 4.8 shows significant differences in surface damage as a function of temperature.
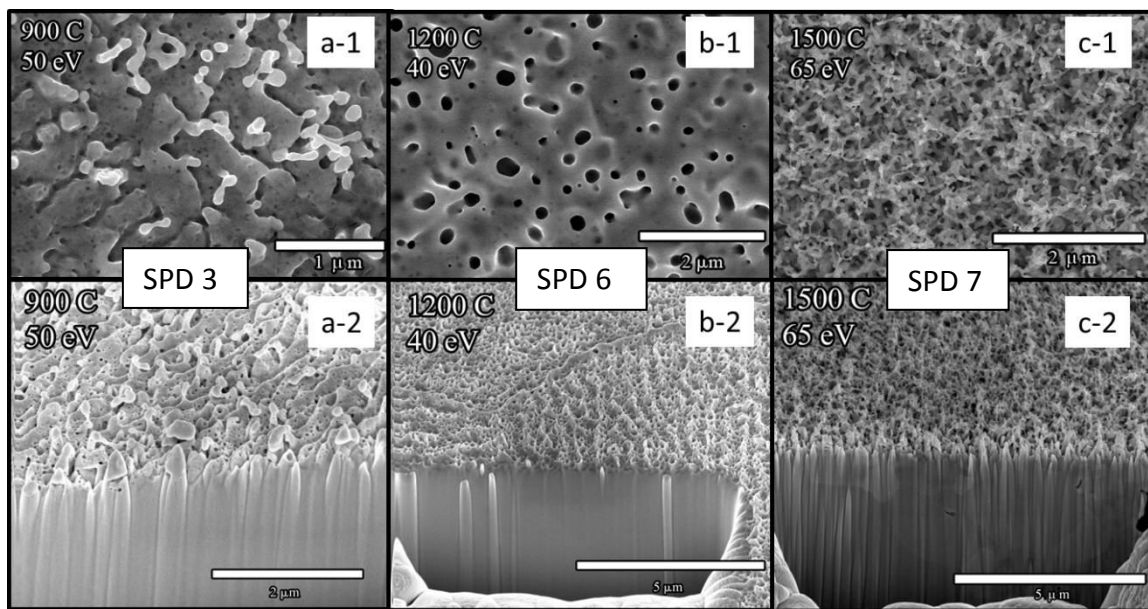
Figure 4.8: SEM images (top) and cross-sectional SEM images (bottom) of SPD tungsten samples 3, 6, and 7 irradiated in Pilot-PSI up to a He plasma fluence ~10^{22} cm^{-2}, presenting the temperature effect on surface morphology and fuzz formation in ultrafine grain tungsten. **(a)** SPD 2 was irradiated at a temperature of 900 °C and ion energy of 50 eV resulting in W nanostructures protruding from surface with small pores. **(b)** SPD 6 was irradiated at a temperature of 1200 °C and energy of 40 eV resulting in a porous, smooth microstructure phase. **(c)** SPD 7 was irradiated at a temperature of 1500 °C and energy of 65 eV resulting in a very thin fiber-form structure indicating initial stages of fuzz formation [75].

All the samples in figure 4.8 were exposed to the same fluence. As temperature is increased, the damage accrued over time also increases. This is seen in 900 °C case: only small pores and surface roughening have occurred. In the 1200 °C case the pores have grown and the surface is beginning to develop tendrils. In the 1500 C case the fuzz has completely formed. This temperature dependence above the threshold temperature is not very surprising, as it is conjectured that thermally activated processes like defect migration are suspected to drive the fuzz growth [18,20,76].

From the previous images, there is strong evidence to suggest that high grain boundary density in SPD tungsten leads to a more radiation resistant material. This prompted a comparison between a SPD sample and MMW sample to see how the MMW sample type faired. Figure 4.9 compares an SPD sample to a MMW sample exposed to similar conditions.
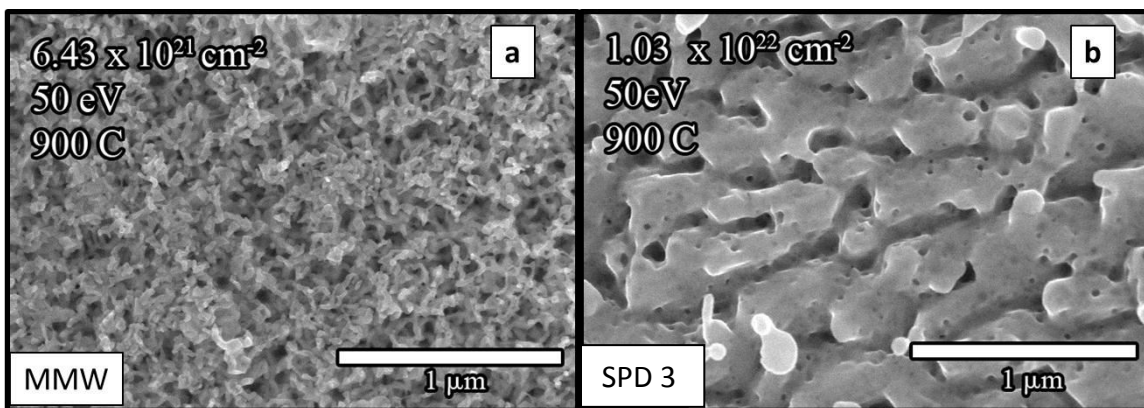
Figure 4.9: Two SEM images comparing irradiation damage in MMW tungsten and SPD tungsten. **(a)** SEM image of MMW tungsten irradiated in Pilot-PSI, located at DIFFER up to a fluence of $6x10^{22}$ cm^{-22}, 50 eV and 900 °C. **(b)** SEM image of SPD 3 irradiated in Pilot-PSI, located at DIFFER up to a fluence of 10^{22} cm^{-2}, 50 eV and 900 °C. MMW tungsten samples quickly reach full fuzz formation below 10^{22} cm^{-2} [75].

Figure 4.9 shows that the SPD sample had less irradiation damage despite being exposed to nearly twice the fluence. Even though the MMW tungsten has a high grain boundary density, it did not improve the fluence threshold for fuzz formation in the same manner as the SPD samples. This is thought to be due to inherent porosity of the samples due to the fabrication method [75].

4.5   *In-situ* TEM studies

The observations made from the SPD samples exposed to high flux, high fluence, low energy helium irradiation served as motivation to elucidate the mechanisms behind fuzz formation and better understand the role grain boundaries play in the resulting morphology evolution. To better understand these phenomena, TEM and *in-situ* TEM analysis were conducted. The standard TEM work on post-irradiated samples was conducted at Birck Nanotechnology Center at Purdue University with a 300 keV JEOL JEM-3010 TEM. The irradiation for these TEM samples took place at DIFFER in their nano-PSI machine detailed in the low fluence studies section. The *in-situ* TEM work was completed in a JEOL JEM-2000FX TEM at the Microscope and Ion Accelerator for Materials Investigation (MIAMI) facility at the University of Huddersfield. The MIAMI facility allowed for real time TEM analysis of SPD tungsten samples during helium ion irradiation. The helium ion energy was 2 keV with a operational flux of 3.3×10^{16} ions.m^{-2}-s^{-1}. Stopping Range of Ions in Matter (SRIM) [77] was used to determine that the stopping range of the helium ions in the tungsten sample is ~10 nm. This is important, as it confirms that the stopping range of the ions is within the nominal characteristic length of the SPD samples. The sample temperature was maintained at 950 °C by the use of a Gatan Model 652 heating holder, with images and video captured using a Gatan ORIUS SC200 digital camera. The images were taken within ±1.5μm of defocus, and the beam energy of the MIAMI TEM was 200 keV.

The sample temperature of 950 °C was chosen because it was consistent with a large portion of the high flux work already completed and because at this temperature the barrier for vacancy [78] and interstitial [79] migration are overcome. As mentioned previously, Bai et al. [65] explained how grain boundaries act as defect sinks; a study by Singh et al. [66] pointed out that He ions trapped in grain boundaries have a large energy barrier to diffuse back into the matrix. This results in an accumulation of helium in the grain boundaries. Thus, it is expected to see less bubble formation within smaller grains and more bubble nucleation at the grain boundaries. Figure 4.10 shows several TEM images taken during *in-situ* irradiation of a SPD tungsten sample. The observations made from this image are consistent with the stated hypothesis.
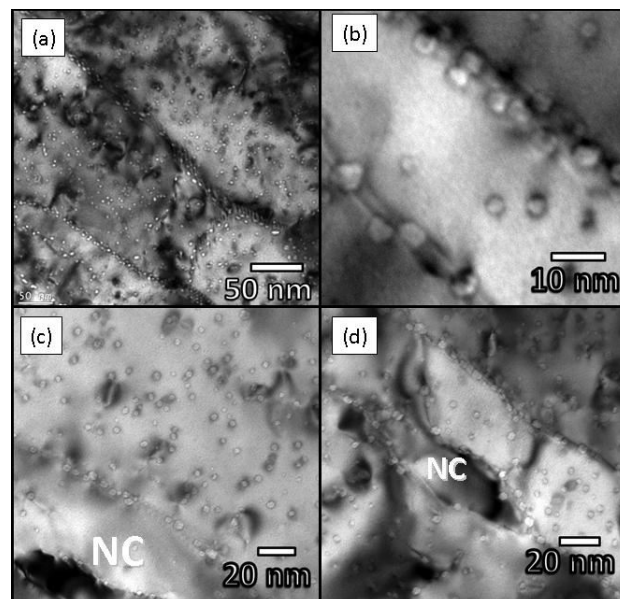
Figure 4.10: Ultrafine and nanocrystalline grains in tungsten after irradiation with 2 keV He$^+$ to a fluence of 3.6×10^{19} ions.m^{-2} at 950°C: (a) overview of typical microstructure of sample; (b) higher magnification micrograph showing grain boundaries decorated with bubbles; and (c)–(d) nanocrystalline grains (denoted NC) demonstrating significantly lower areal densities of bubbles compared to ultrafine grains [80].

As seen in figure 4.10, bubbles are clustering at the grain boundaries and there are

fewer bubbles within nanocrystalline grains (grain size less than 100 nm). This is shown

clearly in figure 4.10(c), where the large grain on top is riddled with bubbles but the thin

grain below only has bubbles at the grain boundary. Bubble nucleation rate and defect

production rate within these smaller grains is observed to be significantly slower than

that of large grain (several microns) and even ultra-fine (less than 500 nm) grains. Figure

4.11 shows a time evolution of a nanocrystalline grain and an ultrafine grain side by side.
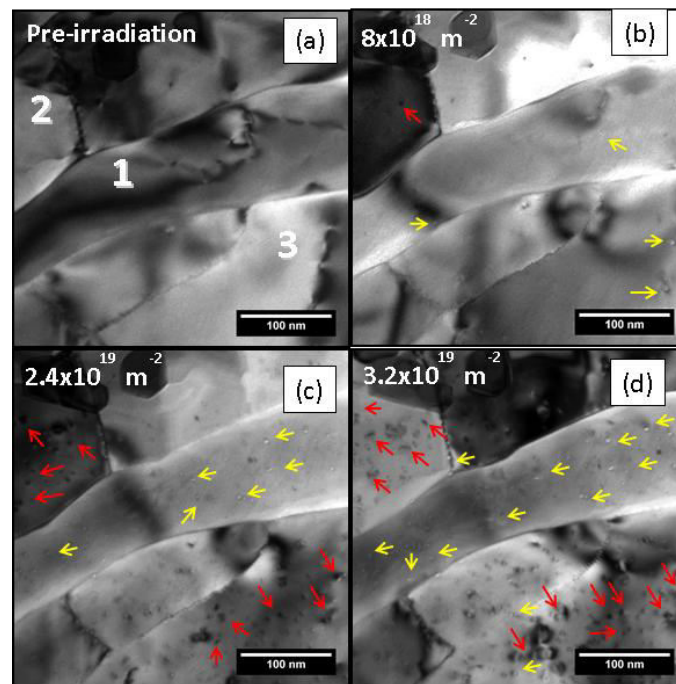
Figure 4.11: TEM micrographs of *in situ* 2 keV He[+] ion irradiation of tungsten at 950°C showing: (a) nanocrystalline (1) and ultrafine (2 and 3) grains before irradiation; (b) at a fluence of 8×10^{18} ions.m^{-2} and after bubble nucleation (bubbles indicated by yellow arrows); (c) after irradiation to a fluence of 2.4×10^{19} ions.m^{-2} showing point defect cluster formation (indicated by red arrows) occurred predominantly in grains 2 and 3; and (d) after irradiation to a fluence of 3.2×10^{19} ions.m^{-2} with a higher areal density of point defect clusters and small dislocation loops evident in grains 2 and 3 whilst grain 1 demonstrates a uniform distribution of bubbles and a significantly lower areal density of defect clusters and dislocation loops. (arrows guide the eye to aid in identifying respective defects)[80].

Figure 4.11 (a)-(d) shows the damage progression and defect production in larger grains to be much faster than that of the nanocrystalline grains. First, bubble formation begins around a fluence of 8x10^{18} ions-cm^{-2}. These appear as small white dots. This is followed by dislocation loop and defect cluster production.

Further investigation of the bubble formation process in varying tungsten grain sizes showed interesting relations between bubble size distribution and grain size. Images taken during the *in-situ* TEM process were used to identify grain sizes and divided them into three categories; grains that were 40-60nm, grains that were 60-100 nm and grains that were greater than 100 nm. Then, the bubbles in each grain were counted and a bubble size distribution was made for each grain size category. Figure 4.12 shows the distributions for the three categories.
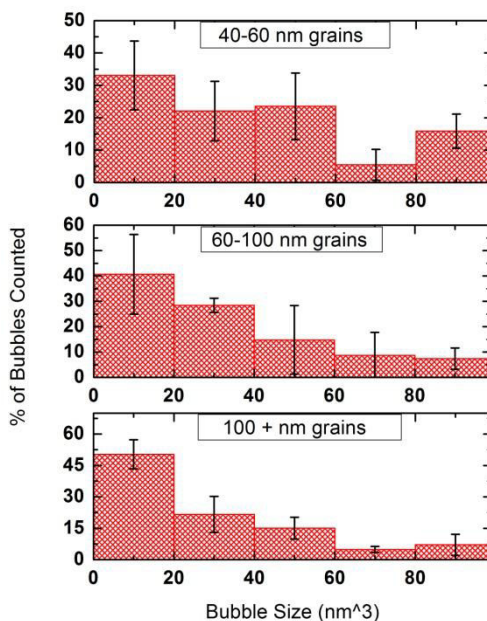
Figure 4.12: Size distributions of bubbles observed in grains of various dimensions at a fluence of 3.2×10^{19} ions.m^{-2}. Bubbles located on grain boundaries were not counted, i.e. only intragranular bubbles are counted [80].

There is not much change in bubble distribution observed between the 60 -100 nm and 100+ nm groups, but there seems to be a significant difference in the bubble size distribution in the 40-60 nm group. The bubbles in this group tend to be larger on average and are much more likely to very large bubbles. This observation is reflected physically in Figure 4.13.
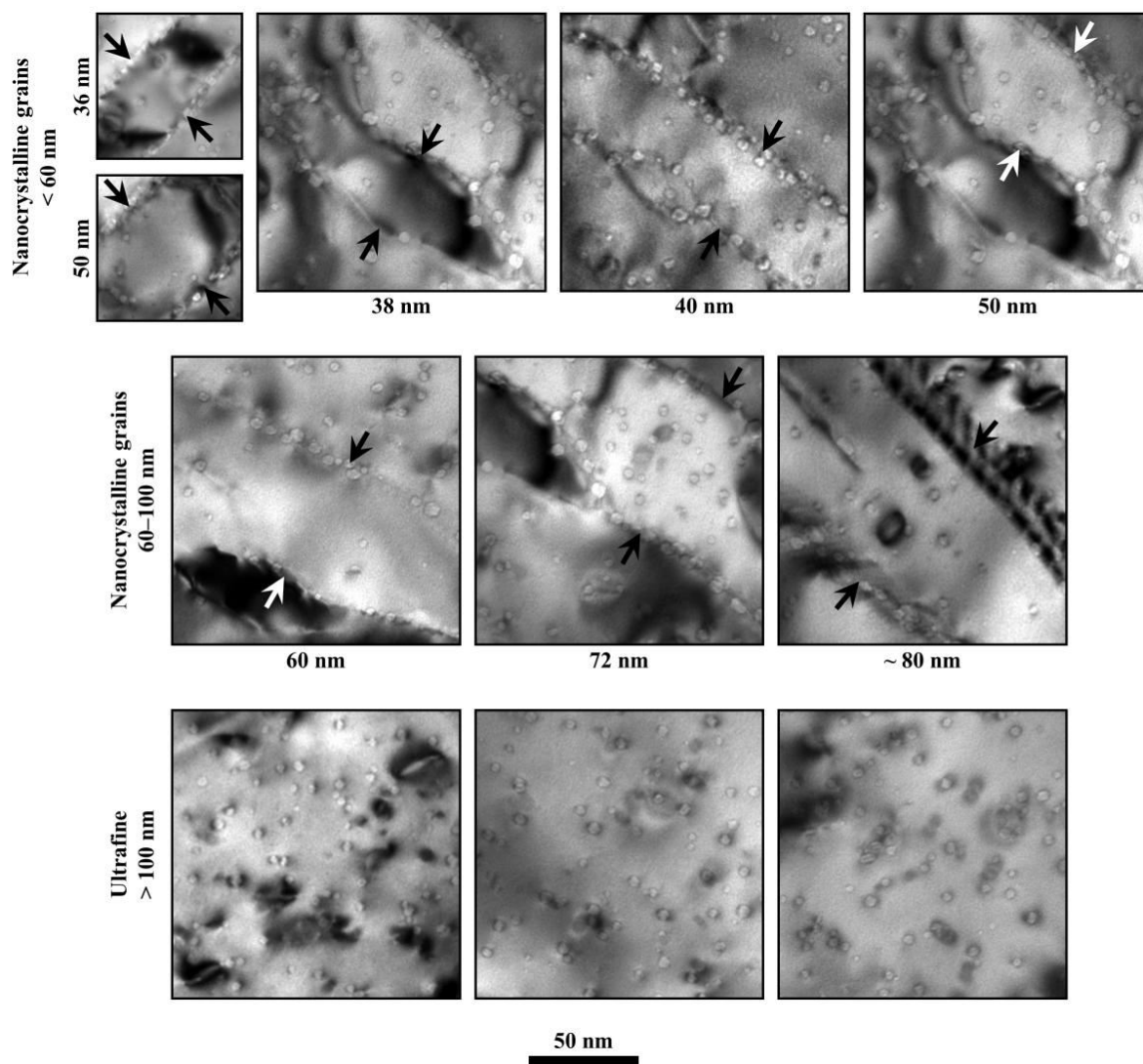
Figure 4.13: TEM micrographs of different grain sizes showing different bubble densities at a fluence of 3.2×10^{19} ions.m^{-2}. Scale marker applies to all micrographs [80].

Figure 4.13 is the pictorial version of the bubble distribution graphs. These images make it clear that the average bubble size is dependent on grain size. The 40 - 60 nm grain size group also showed lower areal bubble density. This is consistent with literature, as the small grains have less helium trapped in them. Essentially, grain boundaries act as a defect sink, making the formation of He-vacancy complexes less likely. Thus, it becomes more likely that the helium will either find an already-formed bubble or it will migrate to the grain boundary.

In addition to bubble formation, defect migration, such as dislocation loop shuttling, was observed during the irradiation process. Figure 4.14 shows a frame-by-frame analysis of this phenomena.
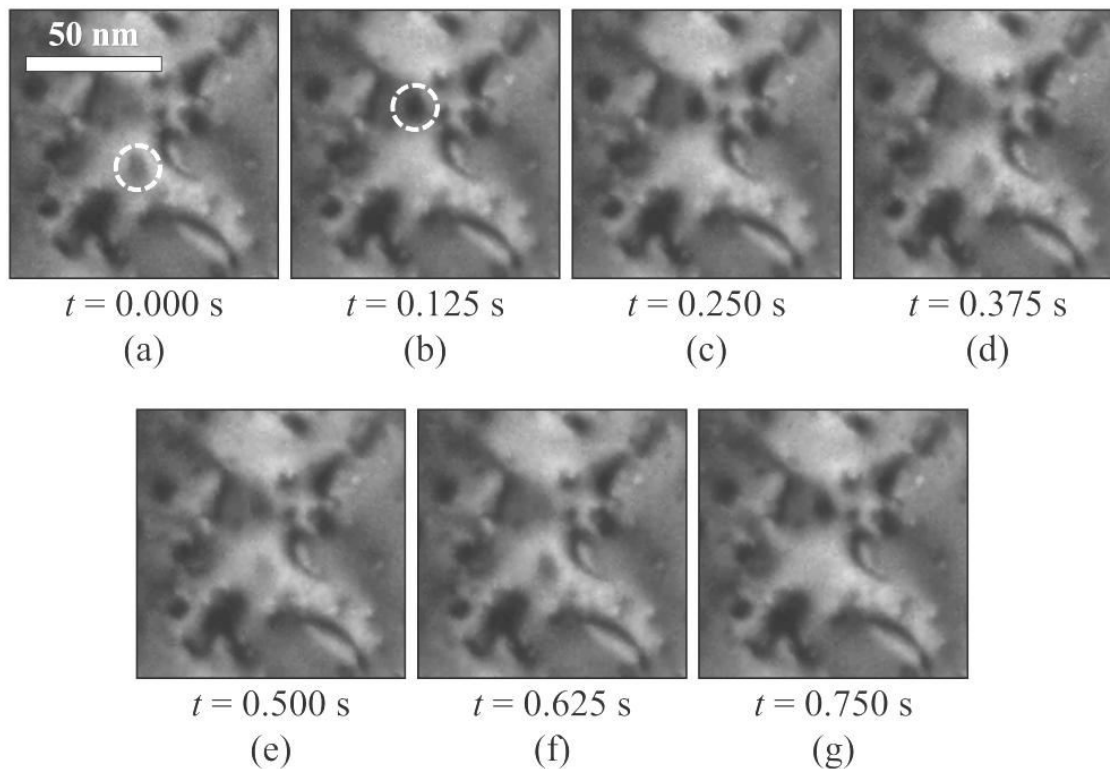
Figure 4.14: Series of consecutive TEM video frames captured at a fluence of 2.8×10^{19} ions.m^{-2} showing a dislocation loop shuttling between two sites indicated by the white dashed circles in (a) and (b). The loop appears to occupy both sites in frames (d) to (f) as the shuttling frequency was greater than the video frame capture rate of 8 Hz. Scale marker in (a) applies to all seven panels [80].

This high defect mobility and production has not been seriously considered to play a major role in the microstructure evolution in tungsten. However, a study by Ohno et al. [81] may suggest some indirect evidence regarding the importance of defect production and mobility. In that study, the crystallographic orientation dictated the structures formed under irradiation. This observation is supported by secondary electron image formed using a Ga^{+} ion beam of an ultrafine-grained sample irradiated with 30 eV He^{+} ions at 1200°C to a fluence of 10^{26} ions.m^{-2}. This image can be seen in Figure 4.15.
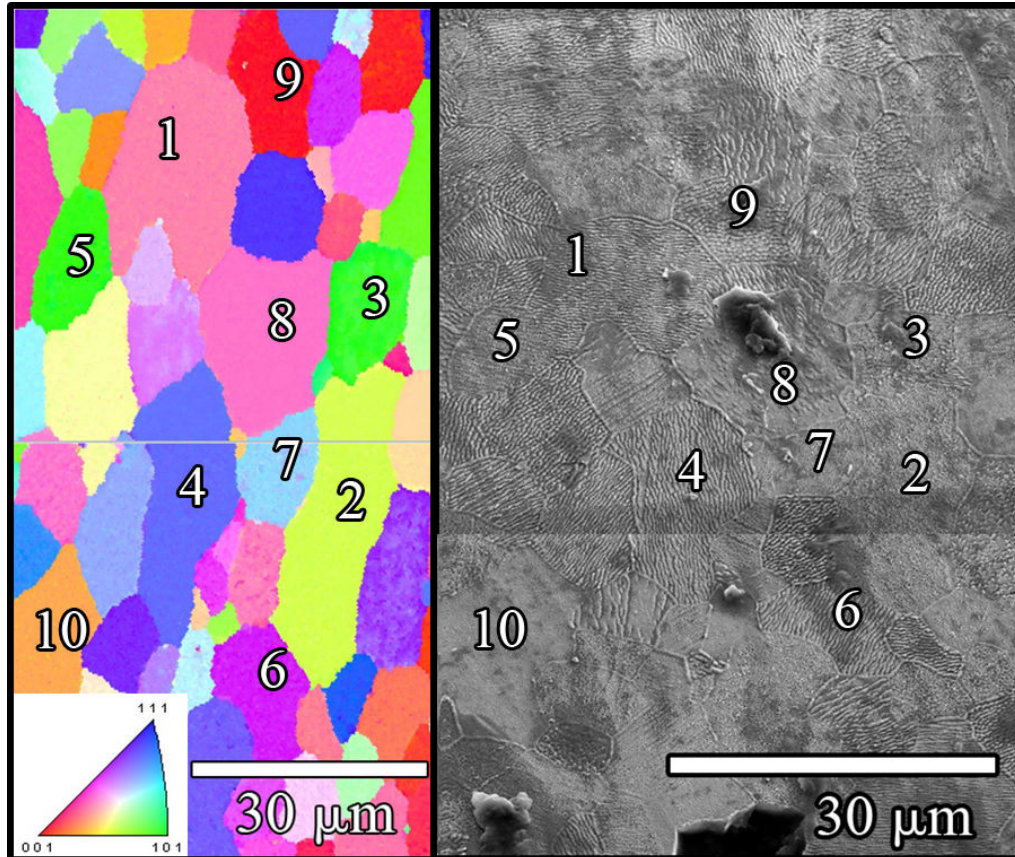
Figure 4.15: EBSD image (left) and SEM image (right) correlating the structures induced via radiation to their grain orientation. The EBSD and the SEM image are from SPD 6 exposed at DIFFER, and were imaged in the same spot. The conditions for SPD 6 have been previously discussed [80].

Figure 4.15 shows how different grain orientations lead to different morphology evolution. If these changes in morphology are affected by grain orientation it suggests that defect production and mobility may play a significant role in the microstructure evolution because defect mobility is dependent on crystallographic structure [81].

TEM analysis of SPD tungsten revealed some key observations regarding the behavior of helium ions once they enter the grains. Large and ultra-fine grains behaved differently from the nanocrystalline grains regarding bubble size, bubble locations, and

defect production. This indicates a strong dependence of grain boundaries on the morphology evolution process. It has been shown that the high grain boundary density slows down bubble nucleation and defect production and is a major reason why SPD tungsten has a higher radiation tolerance. However, with the large amounts of helium going to the grain boundary it would seem that some sort of saturation is occurring. This might explain why fuzz is formed in SPD tungsten, just at a later fluence. Thermal Desorption Spectroscopy (TDS) on SPD samples before and after the formation of fuzz could provide some answers regarding this.

4.6   Chapter Summary

Early stage damage of tungsten surfaces was investigated by examining low flux, low energy, low fluence helium exposures of SPD tungsten samples. The low fluence studies supported conjectures about the strong temperature dependence on damage in tungsten PFCs. However, considerable damage was observed for low fluxes and ion energy considerably below the displacement energy for helium on tungsten. This supports claims that irradiation enhanced effects and temperature enhanced effects are driving the nanostructure formation observed in high fluence studies.

The high fluence work done at DIFFER specifically focused on tungsten samples with different grain boundary densities. The results of these experiments revealed that higher grain boundary density may be connected with less damage accumulation within the material, resulting in the onset of tungsten fuzz at an order of magnitude larger

fluence. Helium bubble nucleation mechanisms combined with grain boundaries absorbing interstitials formed during the irradiation process and later re-emitting them to reduce the number of He-vacancy complexes that can form are suggested theories behind the observed radiation tolerance.

In-situ TEM analysis of SPD tungsten samples undergoing irradiation via high energy helium was conducted as a complementary study to the work completed at DIFFER. *In-situ* results showed a strong dependence on defect production rate and bubble distribution based on grain size. The nano-grains had far less damage and the bubbles were highly concentrated on the grain boundary. This supports other work which suggests that the grain boundaries act as defect sinks. This work was done with high energy He irradiation (2 keV or more) so the results should be taken with caution. Continued TEM work investigating low energy (25-100 eV) ion irradiation is important to correlate the early stage damage accrued in SPD materials to the resultant nanostructure formed after exposure to high fluences.

CHAPTER 5.   FUTURE WORK

The results on SPD tungsten have prompted further investigation into other important characteristics of PFCs, specifically the effect that grain size has on retention properties and thermo-mechanical properties of the material. Further work is already being conducted in these areas. A brief description of the planned work and preliminary results are detailed below.

5.1   TDS analysis on tungsten samples with different grain sizes

Several studies have looked at the deuterium retention in Tungsten from both a damage and plasma performance point of view [82, 83, 84]. In most of these papers, there is a consensus that the retention of D leads to bubble formation, which then burst and release deuterium and alter the surface. This mechanism is confirmed using TDS analysis. However, the role that grain boundary density plays on this mechanism is not heavily investigated. In addition to deuterium retention properties, TDS will allow for a better understanding of how helium is being trapped in tungsten materials exposed to high fluence helium irradiation. Helium bubble formation is fairly well understood, but

there are some major gaps in knowledge in regards to explaining exactly how SPD

tungsten materials appear to be more resistant to irradiation damage. Specifically, fuzz

formation on SPD samples is not prevented, only delayed. This implies that whatever

benefit higher grain boundary materials have, that benefit expires over time.

This calls for a future experiment to be conducted at DIFFER in which a

commercial tungsten sample and a SPD tungsten sample are irradiated to a pre-fuzz

state (~10^{25} ion-m^{-2}) with 30-70eV helium ions at 900 °C. Then, another set of

commercial and SPD samples are irradiated to a post fuzz state (~10^{27} ion-m^{-2}) with 30-

70eV helium ions at 900 °C. This will then be followed by thermal desorption

spectroscopy (TDS) on both sets of samples. The theory presented in this thesis is that

the helium is trapped differently in SPD tungsten. The idea is that the increased grain

boundary density leads to more helium going to the grain boundary, which in turn

reduces the damage production rate in the grains themselves. This difference should

appear in the TDS spectrums when monitoring release of helium from the sample

surface. However, it was shown that this grain boundary effect is only temporary, in the

sense that fuzz nanostructure does eventually form on SPD tungsten samples. This

implies that some saturation effect is taking place. By performing TDS on the post-fuzz

pair of samples, we will see if the TDS spectrum between the commercial and SPD

samples has converged. This would indicate that the grain boundaries are perhaps full,

and no longer able to prevent or reduce damage within the grains.

The use of TDS can also be extended to get interesting results on the retention of

deuterium in SPD tungsten. This would help answer questions about the role of grain

boundaries on retention properties, which will be a concern if these ultrafine grained materials continue to look promising for use in fusion devices.

5.2   Study of ELM-like events on SPD tungsten

Continued collaboration with DIFFER could also open an avenue of work in regard to investigating ELMs effect on SPD tungsten. The Magnum-PSI machine can be used to expose SPD samples to steady state and pulsed plasma loads simultaneously. This would provide interesting data concerning how ultrafine grained materials perform under these spikes in heat flux. This study could include more detailed thermal and mechanical testing of SPD samples before and after steady state (He and/or D) plasma exposure. For example, the study could include use of pre- and post-irradiation nano-indentation. This type of information is important to know, because radiation tolerance is not the only property that is important in PFCs.

LIST OF REFERENCES

LIST OF REFERENCES

[1] Pizzuto, A., et al. "The Fusion Advanced Studies Torus (FAST): a proposal for an ITER satellite facility in support of the development of fusion energy." Nuclear Fusion 50.9 (2010): 095005.

[2] Davis, J. W., et al. "Assessment of tungsten for use in the ITER plasma facing components." Journal of nuclear materials 258 (1998): 308-312.

[3] Ueda, Y., et al. "Research status and issues of tungsten plasma facing materials for ITER and beyond." Fusion Engineering and Design (2014).

[4] Jensen, Roderick V., et al. "Calculations of impurity radiation and its effects on tokamak experiments." Nuclear Fusion 17.6 (1977): 1187.

[5] Meade, Dale M. Effect of high Z impurities on the ignition and Lawson conditions for a thermonuclear reactor. Princeton Univ., NJ (USA). Plasma Physics Lab, 1973.

[6] Neu, R., et al. "Tungsten: an option for divertor and main chamber plasma facing components in future fusion devices." Nuclear fusion 45.3 (2005): 209.

[7] Davis, Joseph R., ed. Properties and selection: nonferrous alloys and special-purpose materials. Vol. 2. Asm Intl, 1990.

[8] Linke, Jochen. "High heat flux performance of plasma facing materials and components under service conditions in future fusion reactors." Fusion Sci. Technol 53 (2008): 278.

[9] Post, Douglass Edmund, et al. "Steady-state radiative cooling rates for low-density, high-temperature plasmas." Atomic data and nuclear data tables 20.5 (1977): 397-439.

[10] Gusev, M. I., et al. "Sputtering of tungsten, tungsten oxide, and tungsten-carbon mixed layers by deuterium ions in the threshold energy region." Technical Physics 44.9 (1999): 1123-1127.

[11] Roth, J., J. Bohdansky, and A. P. Martinelli. "Low energy light ion sputtering of metals and carbides." Radiation Effects 48.1-4 (1980): 213-219.

[12] Pitts, R. A., et al. "Material erosion and migration in tokamaks." Plasma physics and controlled fusion 47.12B (2005): B303.

[13] Eckstein, W., and J. Laszlo. "Sputtering of tungsten and molybdenum." Journal of nuclear materials 183.1 (1991): 19-24.

[14] Winters, H. F., et al. "Chemical Sputtering of Tungsten at Elevated Temperatures." Journal of Applied Physics 34.6 (2004): 1810-1816.

[15] Gorynin, I. V., et al. "Effects of neutron irradiation on properties of refractory metals." Journal of nuclear materials 191 (1992): 421-425.

[16] Steichen, J. M. "Tensile properties of neutron irradiated TZM and tungsten." Journal of Nuclear Materials 60.1 (1976): 13-19.

[17] Shimada, Masashi, et al. "The deuterium depth profile in neutron-irradiated tungsten exposed to plasma." Physica Scripta 2011.T145 (2011): 014051.

[18] Kajita, Shin, et al. "Formation process of tungsten nanostructure by the exposure to helium plasma under fusion relevant plasma conditions." Nuclear Fusion 49.9 (2009): 095005.

[19] Baldwin, M. J., and R. P. Doerner. "Formation of helium induced nanostructure 'fuzz'on various tungsten grades." Journal of Nuclear Materials 404.3 (2010): 165-173.

[20] Doerner, R. P., M. J. Baldwin, and P. C. Stangeby. "An equilibrium model for tungsten fuzz in an eroding plasma environment." Nuclear Fusion 51.4 (2011): 043001.

[21] Wright, G. M., et al. "Tungsten nano-tendril growth in the Alcator C-Mod divertor." Nuclear Fusion 52.4 (2012): 042003.

[22] Wang, Wenmin, et al. "Blister formation of tungsten due to ion bombardment." Journal of nuclear materials 299.2 (2001): 124-131.

[23] Tokunaga, K., et al. "Blister formation and deuterium retention on tungsten exposed to low energy and high flux deuterium plasma." Journal of nuclear materials 337 (2005): 887-891.

[24] Alimov, V. Kh, et al. "Surface morphology and deuterium retention in tungsten exposed to low-energy, high flux pure and helium-seeded deuterium plasmas." Physica Scripta 2009.T138 (2009): 014048.

[25] Doerner, R. P., et al. "Codeposition of deuterium with ITER materials." Nuclear Fusion 49.3 (2009): 035002.

[26] Luo, G-N., W. M. Shu, and M. Nishi. "Incident energy dependence of blistering at tungsten irradiated by low energy high flux deuterium plasma beams." Journal of nuclear materials 347.1 (2005): 111-117.

[27] Iwakiri, H., et al. "Microstructure evolution in tungsten during low-energy helium ion irradiation." Journal of nuclear materials 283 (2000): 1134-1138.

[28] Yoshida, Naoaki, et al. "Impact of low energy helium irradiation on plasma facing metals." Journal of nuclear materials 337 (2005): 946-950.

[29] Nishijima, Dai, et al. "Formation mechanism of bubbles and holes on tungsten surface with low-energy and high-flux helium plasma irradiation in NAGDIS-II." Journal of nuclear materials 329 (2004): 1029-1033.

[30] Nishijima, D., et al. "Incident ion energy dependence of bubble formation on tungsten surface with low energy and high flux helium plasma irradiation." Journal of nuclear materials 313 (2003): 97-101.

[31] Baldwin, M. J., and R. P. Doerner. "Helium induced nanoscopic morphology on tungsten under fusion relevant plasma conditions." Nuclear Fusion 48.3 (2008): 035001.

[32] Ueda, Y., et al. "Helium effects on tungsten surface morphology and deuterium retention." Journal of Nuclear Materials 442.1 (2013): S267-S272.

[33] Kajita, Shin, et al. "TEM observation of the growth process of helium nanobubbles on tungsten: Nanostructure formation mechanism." Journal of Nuclear Materials 418.1 (2011): 152-158.

[34] Miyamoto, M., et al. "In situ transmission electron microscope observation of the formation of fuzzy structures on tungsten." Physica Scripta 2014.T159 (2014): 014028.

[35] Nagata, S., and K. Takahiro. "Effect of helium irradiation on trapping and thermal release of deuterium implanted in tungsten." Journal of nuclear materials 290 (2001): 135-139.

[36] Kajita, Shin, et al. "Helium plasma irradiation on single crystal tungsten and undersized atom doped tungsten alloys." Physica Scripta 89.2 (2014): 025602.

[37] Baldwin, M. J., and R. P. Doerner. "Formation of helium induced nanostructure 'fuzz'on various tungsten grades." Journal of Nuclear Materials 404.3 (2010): 165-173.

[38] Iwakiri, H., et al. "Hardening behavior of molybdenum by low energy He and D ion irradiation." Journal of nuclear materials 258 (1998): 873-878.

[39] Watanabe, Y., et al. "Formation of interstitial loops in tungsten under helium ion irradiation: Rate theory modeling and experiment." Nuclear Instruments and Methods in Physics Research Section B: Beam Interactions with Materials and Atoms 255.1 (2007): 32-36.

[40] Odette, G. R., P. J. Maziasz, and J. A. Spitznagel. "Fission-fusion correlations for swelling and microstructure in stainless steels: Effect of the helium to displacement per atom ratio." Journal of Nuclear Materials 104 (1981): 1289-1303.

[41] Kornelsen, E. V. "Entrapment of helium ions at (100) and (110) tungsten surfaces." Canadian Journal of Physics 48.23 (1970): 2812-2823.

[42] Caspers, L. M., A. Van Veen, and T. J. Bullough. "A simulation study of the initial phase of he precipitation in metals." Radiation effects 78.1-4 (1983): 67-76.

[43] Van der Kolk, G. J., et al. "Binding of helium to metallic impurities in tungsten; experiments and computer simulations." Journal of Nuclear Materials 127.1 (1985): 56-66.

[44] Baldwin, M. J., and R. P. Doerner. "Helium induced nanoscopic morphology on tungsten under fusion relevant plasma conditions." Nuclear Fusion 48.3 (2008): 035001.

[45] Kajita, Shin, et al. "TEM observation of the growth process of helium nanobubbles on tungsten: Nanostructure formation mechanism." Journal of Nuclear Materials 418.1 (2011): 152-158.

[46] Miyamoto, M., et al. "In situ transmission electron microscope observation of the formation of fuzzy structures on tungsten." Physica Scripta 2014.T159 (2014): 014028.

[47] Nagata, S., and K. Takahiro. "Effect of helium irradiation on trapping and thermal release of deuterium implanted in tungsten." Journal of nuclear materials 290 (2001): 135-139.

[48] Ueda, Y., et al. "Exposure of tungsten nano-structure to TEXTOR edge plasma." Journal of Nuclear Materials 415.1 (2011): S92-S95.

[49] Tokitani, M., et al. "Exfoliation of the tungsten fibreform nanostructure by unipolar arcing in the LHD divertor plasma." Nuclear Fusion 51.10 (2011): 102001.

[50] Gibson, James, David Armstrong, and Steve Roberts. "The micro-mechanical properties of ion irradiated tungsten." Physica Scripta 2014.T159 (2014): 014056.

[51] Allain, Jean Paul, and Chase N. Taylor. "Lithium-based surfaces controlling fusion plasma behavior at the plasma-material interfacea)." Physics of Plasmas (1994-present) 19.5 (2012): 056126.

[52] Taylor, C. N., et al. "Materials analysis and particle probe: A compact diagnostic system for in situ analysis of plasma-facing components (invited) a)." Review of Scientific Instruments 83.10 (2012): 10D703.

[53] Hirooka, Yoshi. "Review of beryllium and tungsten erosion behavior and universal modeling of plasma impurity effects observed in recent PISCES experiments." Physica Scripta 1996.T64 (1996): 84.

[54] Ohno, Noriyasu, et al. "Development of Divertor Plasma Simulators with High Heat Flux Plasmas and its Application to Nuclear Fusion Study: A Review." IEEJ Transactions on Electrical and Electronic Engineering 4.4 (2009): 476-487.

[55] de Groot, B., et al. "Magnum-psi, a new linear plasma generator for plasma-surface interaction studies in ITER relevant conditions." Fusion engineering and design 66 (2003): 413-417.

[56] Kroesen, G. M. W., D. C. Schram, and J. C. M. De Haas. "Description of a flowing cascade arc plasma." Plasma Chemistry and Plasma Processing 10.4 (1990): 531-551.

[57] De Temmerman, G., et al. "ELM simulation experiments on Pilot-PSI using simultaneous high flux plasma and transient heat/particle source." Nuclear Fusion 51.7 (2011): 073008.

[58] De Temmerman, G., et al. "High heat flux capabilities of the Magnum-PSI linear plasma device." Fusion Engineering and Design 88.6 (2013): 483-487.

[59] J. A. Hinks, J. A. Van den Berg, S. E. Donnelly, J. Vac. Sci, Technol. A 29 (2011) 021003

[60] Federici, Gianfranco, et al. "Plasma-material interactions in current tokamaks and their implications for next step fusion reactors." Nuclear Fusion 41.12 (2001): 1967.

[61] Buzhinskij, O. I., and Yu M. Semenets. "Thick boron carbide coatings for protection of tokamak first wall and divertor." Fusion Engineering and design 45.4 (1999): 343-360.

[62] Makhankov, A., et al. "Performance of the different tungsten grades under fusion relevant power loads." Journal of nuclear materials 290 (2001): 1117-1122.

[63] Wei, Q., et al. "Mechanical behavior and dynamic failure of high-strength ultrafine grained tungsten under uniaxial compression." Acta Materialia 54.1 (2006): 77-87.

[64] Faleschini, M., et al. "Fracture toughness investigations of tungsten alloys and SPD tungsten alloys." Journal of Nuclear Materials 367 (2007): 800-805.

[65] Bai, Xian-Ming, et al. "Efficient annealing of radiation damage near grain boundaries via interstitial emission." Science 327.5973 (2010): 1631-1634.

[66] Singh, Bachu Narain, and A. J. E. Foreman. "Calculated grain size-dependent vacancy supersaturation and its effect on void formation." Philosophical Magazine 29.4 (1974): 847-858.

[67] Samaras, M., et al. "Radiation damage near grain boundaries." Philosophical Magazine 83.31-34 (2003): 3599-3607.

[68] Demkowicz, M. J., R. G. Hoagland, and J. P. Hirth. "Interface structure and radiation damage resistance in Cu-Nb multilayer nanocomposites." Physical review letters 100.13 (2008): 136102.

[69] El-Atwani, Osman, et al. "Multimodal grain size distribution and high hardness in fine grained tungsten fabricated by spark plasma sintering." Materials Science and Engineering: A 528.18 (2011): 5670-5677.

[70] Efe, Mert, et al. "Microstructure refinement of tungsten by surface deformation for irradiation damage resistance." Scripta Materialia 70 (2014): 31-34.

[71] Evans, J. H. "The role of implanted gas and lateral stress in blister formation mechanisms." Journal of Nuclear Materials 76 (1978): 228-234.

[72] J. Delafond, C. Jaouen, J.P. Rivière, C. Fayoux, Mater. Sci. Eng., 69 (1985) 117-121

[73] Van de Sanden, M. C. M., et al. "A combined Thomson–Rayleigh scattering diagnostic using an intensified photodiode array." Review of scientific instruments 63.6 (1992): 3369-3377.

[74] Westerhout, Jeroen, et al. "PSI research in the ITER divertor parameter range at the FOM PSI-lab." Physica Scripta 2007.T128 (2007): 18.

[75] El-Atwani, O., et al. "Ultrafine tungsten as a plasma-facing component in fusion devices: effect of high flux, high fluence low energy helium irradiation." Nuclear Fusion 54.8 (2014): 083013.

[76] De Temmerman, Gregory, et al. "Nanostructuring of molybdenum and tungsten surfaces by low-energy helium ions." Journal of Vacuum Science & Technology A 30.4 (2012): 041306.

[77] Ziegler, James F., M. D. Ziegler, and J. P. Biersack. "SRIM–The stopping and range of ions in matter (2010)." Nuclear Instruments and Methods in Physics Research Section B: Beam Interactions with Materials and Atoms 268.11 (2010): 1818-1823.

[78] Balluffi, R. W. "Vacancy defect mobilities and binding energies obtained from annealing studies." Journal of Nuclear Materials 69 (1978): 240-263.

[79] Dausinger, F., and H. Schultz. "Long-range migration of self-interstitial atoms in tungsten." Physical Review Letters 35.26 (1975): 1773.

[80] El-Atwani, O., et al. "In-situ TEM observation of the response of ultrafine-and nanocrystalline-grained tungsten to extreme irradiation environments." Scientific reports 4 (2014).

[81] Ohno, Noriyasu, et al. "Influence of crystal orientation on damages of tungsten exposed to helium plasma." Journal of Nuclear Materials 438 (2013): S879-S882.

[82] Eleveld, H., and A. van Veen. "Deuterium interaction with impurities in tungsten studied with TDS." Journal of nuclear materials 191 (1992): 433-438.

[83] Shu, W. M., E. Wakai, and T. Yamanishi. "Blister bursting and deuterium bursting release from tungsten exposed to high fluences of high flux and low energy deuterium plasma." Nuclear Fusion 47.3 (2007): 201.

[84] Tokunaga, K., et al. "Blister formation and deuterium retention on tungsten exposed to low energy and high flux deuterium plasma." Journal of nuclear materials 337 (2005): 887-891.